Palaeogeography, Palaeoclimatology, Palaeoecology 569 (2021) 110310

Contents lists available at ScienceDirect

Palaeogeography, Palaeoclimatology, Palaeoecology

journal homepage: www.elsevier.com/locate/palaeo

Minor changes in biomarker assemblages in the aftermath of the Cretaceous-Paleogene mass extinction event at the Agost distal section (Spain)

Claudia Sosa-Montes de Oca [a,b,1,*], Marta Rodrigo-Gámiz [a,c,1], Francisca Martínez-Ruiz [d], Francisco J. Rodríguez-Tovar [a], José Manuel Castro [c], M. Luisa Quijano [e,1], Richard D. Pancost [b]

[a] Departamento de Estratigrafía y Paleontología, Universidad de Granada, Avda. Fuentenueva s/n, 18002 Granada, Spain
[b] Organic Geochemistry Unit, The Cabot Institute for the Environment, School of Earth Sciences, School of Chemistry, University of Bristol, BS8 1TS, UK
[c] Departamento de Geología and CEACTEMA, Universidad de Jaén, Campus Las Lagunillas, 23071 Jaén, Spain
[d] Instituto Andaluz de Ciencias de la Tierra (IACT), CSIC-Universidad de Granada, Avda. Las Palmeras 4, 18100 Armilla, Granada, Spain
[e] Departamento de Química Inorgánica y Orgánica and CEACTEMA, Universidad de Jaén, Campus Las Lagunillas, 23071 Jaén, Spain

ARTICLE INFO

Editor: Shucheng Xie.

Keywords:
Cretaceous/Paleogene boundary
Organic matter sources
Phytoplankton and bacterial communities
High-resolution paleoenvironmental reconstruction
Thermal maturity

ABSTRACT

The Cretaceous/Palaeogene Boundary (KPgB) represents one of the five major mass extinctions in Earth's history, and determining the nature of associated environmental change and biotic recovery is critical for understanding the history of life on our planet. To explore that, we examined the distributions of selected biomarkers (*n*-alkanes, acyclic isoprenoids, steranes and hopanes), organic and carbonate $\delta^{13}C$ values, total organic carbon contents and major and trace elements in a distal section spanning the KPgB (Agost, SE Spain). The studied Agost section is an ~32 cm-thick bathyal sequence of marlstones, clays and marly limestones, and high sedimentation rates allow high (cm) resolution analysis. These analyses exhibit sample-to-sample variability, but there are few significant differences between pre- and post-KPgB biomarker assemblages, suggesting a rapid recovery of the non-fossilizing phytoplankton community after the KPgB. Despite the persistence of life, the organic matter assemblage is rather variable through the first 10 kyr after the impact event. This interval is associated with changing terrigenous and petrogenic inputs as well as varying redox conditions as reflected by the enrichment factor of uranium (U_{EF}) vs that of molybdenum (Mo_{EF}) as well as biomarker indices (gammacerane and homohopane indices). Moreover, sterane distributions do differ between pre- and post-KPgB sediments. Thus, the KPgB impact did affect environmental conditions and non-fossilizing algal and bacterial communities even in distal sites, but these organisms appear to have rapidly recovered, within 10 kyr after the KPgB.

1. Introduction

The mass extinction marking the Cretaceous/Paleogene boundary (KPgB), ~ 66.021 ± 0.024 million years ago (Clyde et al., 2016; Renne et al., 2013; Sprain et al., 2019) was one of the most devastating events in the history of life, associated with the disappearance of about 70% of marine and continental species (D'Hondt, 2005), and it is the most recent and well studied of the 'big five' Phanerozoic mass extinctions. Currently, the relationship between the Cretaceous/Paleogene mass extinction and a meteorite impact is broadly accepted (Hull et al., 2020; Gulick et al., 2019; Pälike, 2013; Schulte et al., 2010), with direct evidence coming from the Chicxulub impact crater, discovered at the beginning of the 1990's on the Yucatán Peninsula in Mexico (Hildebrand et al., 1991). However, alternative or complementary mechanisms, especially volcanism associated with the Deccan Traps, are still considered (Schoene et al., 2019, 2015; Sprain et al., 2019). After decades of research, one of the most critical lines of inquiry is understanding the short- to long-term effects of the Chicxulub impact on the global environmental system, including the time frame required for the re-establishment of pre-impact environmental conditions and marine biological productivity (Bralower et al., 2020; Gulick et al., 2019; Lowery et al., 2020, 2018; Lyons et al., 2020; Rodríguez-Tovar et al.,

* Corresponding author at: Departamento de Estratigrafía y Paleontología, Universidad de Granada, Avda. Fuentenueva s/n, 18002 Granada, Spain.
E-mail addresses: claudia.sosamontesdeoca@bristol.ac.uk (C. Sosa-Montes de Oca), martarodrigo@ugr.es (M. Rodrigo-Gámiz), fmruiz@ugr.es (F. Martínez-Ruiz), fjrtovar@ugr.es (F.J. Rodríguez-Tovar), jmcastro@ujaen.es (J.M. Castro), lquijano@ujaen.es (M.L. Quijano), r.d.pancost@bristol.ac.uk (R.D. Pancost).
[1] Indicates equal author contributions.

https://doi.org/10.1016/j.palaeo.2021.110310
Received 30 September 2020; Received in revised form 9 February 2021; Accepted 16 February 2021
Available online 23 February 2021

2020; Schaefer et al., 2020; Sepúlveda et al., 2019).

There are numerous sites worldwide where the KPgB has been recorded (e.g. Schulte et al., 2010), but the characteristics of these sections differ depending on the distance from the Chicxulub crater. Four types of ejecta deposits have been distinguished: very proximal (e.g. Guayal, Bochil, Moncada, IODP Site 364), proximal (e.g. Beloc, El Mimbral, Brazos River), intermediate (e.g. Sugarite, Starkville South, ODP Leg 171 Sites 1049, 1050, 1052) and distal (e.g. Gubbio, El Kef, Agost and Caravaca). In all of them, major geochemical anomalies have been recognized, but the extraterrestrial contribution is particularly evident in the ejecta layer of distal marine deposits. These sites are also particularly important for assessing the global (as opposed to proximal) consequences of the KPgB and the nature of environmental and biotic recovery.

In particular, the Agost marine distal section in southeast Spain is one of the most continuous, well-preserved, and well-studied KPgB sections in the world (e.g. Molina et al., 2005; Rodríguez-Tovar et al., 2006). Our previous studies of sections in Spain (Caravaca and Agost) (Sosa-Montes de Oca et al., 2013, 2016, Sosa-Montes de Oca et al., 2018a,b, Sosa-Montes de Oca et al., 2020) and Italy (Bottaccione and Contessa) (Sosa-Montes de Oca et al., 2017) have revealed the paleoenvironmental conditions before, during, and after the KPgB impact. Inorganic geochemistry and ichnological analyses on the Agost section revealed variations in bottom water oxygenation, documenting that anoxic conditions were exclusively linked to the ejecta layer produced at the event and that oxic conditions were re-established almost instantaneously, allowing the macrobenthic community to quickly recolonize the substrate (Laska et al., 2017; Rodríguez-Tovar, 2005; Rodríguez-Tovar et al., 2006, 2004; Rodríguez-Tovar and Uchman, 2006, 2004; Sosa-Montes de Oca, 2018).

Many different microorganisms became extinct at the KPgB; among them, marine Cretaceous calcareous nannoplankton were particularly impacted (Alvarez et al., 2019; Lowery et al., 2018; Vellekoop et al., 2019). However, it remains unclear how the non-fossilizing algal and microbial communities were affected. In fact, there have been relatively few reconstructions of changes in organic matter sources through the KPgB at any site (Lowery et al., 2020; Lyons et al., 2020; Schaefer et al., 2020; Sepúlveda et al., 2009) and those performed are often at a very low resolution (Taylor et al., 2018). Biomarkers preserved in sedimentary sequences and structurally linked to specific biological sources (e.g. Eglinton and Eglinton, 2008; Peters et al., 2005), are powerful tools for exploring biotic changes, especially in algal and microbial communities (Grice et al., 2005; Xie et al., 2010). Moreover, biomarker degradation and alteration is governed by environmental conditions, such that they can be also used to reconstruct a wide range of paleoenvironmental conditions (e.g. Eglinton and Eglinton, 2008; Peters et al., 2005).

Previous studies on the KPgB have used different biomarkers to reconstruct organic matter sources, terrestrial plant distributions or seawater temperatures in a small number of very proximal [i.e. IODP Site 364 (Chicxulub); Hull et al., 2020; Lyons et al., 2020] proximal [i.e. Brazos River (Texas-USA), and Beloc (Haiti); Mizukami et al., 2014, Vellekoop et al., 2016, 2014] and distal sections [i.e. Caravaca (Spain), El Kef (Tunisia), Stevns Klint, (Denmark), mid-Waipara River (New Zealand) and Seymour Island (Antartica); Mizukami et al., 2013; Scasso et al., 2020, 2005; Sepúlveda et al., 2009; Taylor et al., 2018; Vellekoop et al., 2015]. Applications of specific biomarkers to explore post-KPgB changes in biotic assemblages are even more limited. Recently, Schaefer et al. (2020) used lipid biomarker analyses at the Chicxulub crater core material (IODP Site 364) to reveal a rapid recovery of microbial life. Similarly, Bralower et al. (2020a) analyzed the micrite-rich layer (boundary clay) at 31 sites across the world, from very proximal to distal locations and through a range of depths in all ocean basins, revealing abundant bacterial and eukaryotic algal biomarkers; they conclude that most micrite in the carbonate layer at distal sites was produced by ocean-wide blooms of cyanobacteria and algae in the millennia after the KPgB impact event. Similarly, Sepúlveda et al. (2009) used sterane distributions to argue for blooms of algae and other non-fossilizing phytoplankton just above the boundary in the Fish Clay of Denmark (Stevns Klint distal section), and then a rapid recovery to pre-event distributions. However, biotic and environmental responses are likely to be highly variable spatially, and obtaining further records is critical to understanding post-impact biotic recovery.

Here, we present a continuous cm-scale resolution and multiproxy analysis across ~32 cm-thick KPgB interval at the Agost distal section (SE Spain) that spans the ~24 kyr following the KPgB event (Groot et al., 1989). Combined with C-isotope and major and trace element profiles (Ca/Al, K/Al, Mg/Al, Cr/Al, Ni/Al, Cu/Al, Zn/Al, Rb/Al, Zr/Al, U/Al and Mo/Al ratios), the distribution of specific phytoplankton (e.g. pristane, phytane, steranes) and bacterial (hopanes) biomarkers at the Agost section allows us to: i) determine changes in the organic matter (OM) inputs before and in the immediate aftermath of the extinction; ii) examine the thermal maturity of the source rocks (changes that likely reflect reworked sedimentary OM inputs in this section); iii) evaluate photosynthetic productivity variations and changes in algal/microbial assemblages across the KPgB event; and most importantly iv) reconstruct how long it took for these interlinked processes to recover after the impact event.

2. Geological setting

The distal KPgB section of Agost (38°27′3.31′N; 0°38′9.71″E) is located at km 9 of road CV-827 (West side), North of the town of Agost, Alicante (southeast Spain) (Fig. 1). At the time of the KPgB impact, the Agost site was located in an upper-bathyal setting (~600 to 1000 m depth) (Schulte et al., 2010) at around 27–30° N palaeolatitude (Van Hinsbergen et al., 2015).

Lithologically, the Agost section comprises a succession of four units (Fig. 1) (see Sosa-Montes de Oca et al., 2018a,b, Sosa-Montes de Oca et al., 2020, for details): the Cretaceous sediments that consist of gray calcareous marlstones and marlstones from the late Maastrichtian (unit a); the overlying Paleogene sediments with a 2–3 mm thick red clay (the ejecta layer; unit b) overlain by a blackish-gray clay layer (the boundary clay; unit c) with gradually increasing carbonate contents related to the recovery of biological productivity; and finally the typical light marly limestones of the early Danian (unit d). The ejecta layer, at the distal sections, marks the sharp contrast between the Maastrichtian and Danian, and contains impact evidence such as spherules (Glass and Burns, 1987; Smit, 1999; Smit and Klaver, 1981), iridium and other platinum-group element anomalies (Alvarez et al., 1980, 1990), elevated concentrations of Cr, Fe, Ni, and Ti which may have come from the meteorite, a sulphide-rich carbonaceous chondrite (Kyte, 1998; Martínez-Ruiz et al., 1997; Shukolyukov and Lugmair, 2004), and a significant decrease in Ca due to the mass extinction among pelagic calcifiers (Goderis et al., 2013; Schulte et al., 2010).

According to the magnetostratigraphy-derived sedimentation rates (Groot et al., 1989) – estimated to be 1.98 cm kyr^{-1} for the uppermost Maastrichtian sediments and calculated to be 0.83 cm kyr^{-1} for the lowermost Danian sediments – the ~32 cm-thick KPgB interval at Agost is thought to span a time interval of ~29 kyr, ranging from 5 kyr before to 24 kyr after the KPgB. Furthermore, it is thought that the ejecta layer deposition itself was a snapshot on a geological time scale, potentially, on the order of days to months (Artemieva and Morgan, 2009).

3. Materials and methods

3.1. Core description and sampling

A ~ 32 cm-thick bore hole was drilled in the Agost section on May of 2017 to obtain a complete and continuous record of the KPgB interval with the four-above-mentioned units (a, b, c and d, see Fig. 1), ranging from the uppermost Maastrichtian to the lowermost Danian. A fresh/unexposed and intact KPgB section was recovered using a Rolatec RL 48

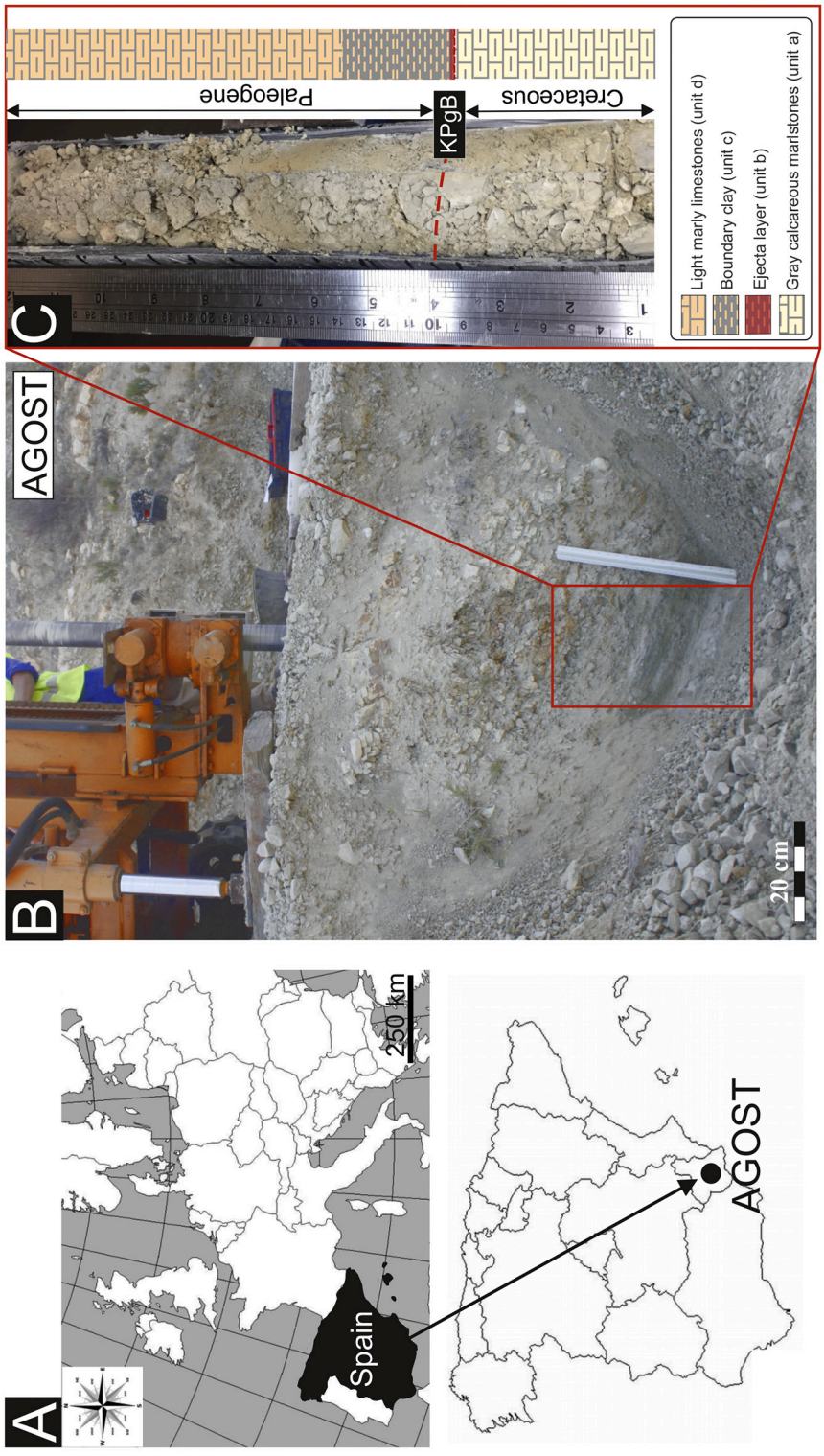

Fig. 1. The Agost outcrop and KPgB section. A-Location of the Cretaceous-Paleogene (KPg) section at the Agost site (Alicante, Southeast Spain). B- Photograph of the section taken during drilling. C-Detail of the KPgB recovered core, comprising: (unit a) gray calcareous marlstones and marlstones from the uppermost Maastrichtian, (unit b) 2 mm-thick ejecta layer, (unit c) blackish-gray boundary clay layer and (unit d) the light marly limestones, the last three belonging to the lowermost Danian. Modified from Sosa-Montes de Oca et al. (2018a).

L drilling machine with rubber tracks from the Center for Scientific Instrumentation (CIC) at the University of Granada (Spain). Details about the extraction methodology were previously presented in Sosa-Montes de Oca (2018) and Sosa-Montes de Oca et al. (2018a). Once the core was obtained, it was sealed and stored at 4 °C in a cold room.

The ~32 cm-thick of the KPgB core was sampled continuously each 1 to 2 cm depending of the unit interval (~20 g were taken for the Maastrichtian and Danian samples and ~ 0.001 g for both KPg boundary samples), yielding a total of 22 samples for inorganic geochemical analyses, 16 samples for biomarker analyses and 20 samples for total organic carbon and organic and carbonate $\delta^{13}C$ analyses. Specifically, 7 samples were taken in the 10 cm from the gray calcareous marlstones of late Maastrichtian age (unit a), and 15 samples were taken from the lower 22 cm of the early Danian, the latter comprising: 2 samples from the 2 mm-thick ejecta layer (unit b), with only enough material to determine major and trace elements analyses; 5 samples from the 5 cm-thick boundary clay layer (unit c); and 8 samples from the 15 cm-thick light marly limestones (unit d).

3.2. Inorganic geochemistry

3.2.1. ICP-OES and ICP-MS analyses

Inorganic geochemical analyses were conducted on 22 samples crushed in an agate mortar and digested with nitric acid (HNO_3) and hydrofluoric acid (HF) in order to obtain the sample solution. Trace element concentrations were determined using ICP-Mass Spectrometry (NEXION 300D). Results were calibrated using blanks and international standards, with analytical precision better than ±2% for 50 ppm elemental concentrations and ± 5% for 5 ppm elemental concentrations. The concentrations of major elements (Al, Ca, Fe, K and Mg) were measured in the same sample solutions using an ICP-Optical Emission Spectroscope (Perkin-Elmer Optima 8300) with a Rh anode X-ray tube. Blanks and international standards were used for quality control and the analytical precision was better than ±2.8% and 1.9% for 50 ppm elemental concentrations of Al and Ca, respectively; better than ±0.5% for 20 ppm elemental concentrations of Fe; better than ±0.4% for 5 ppm elemental concentrations of K; and better than ±1.5% for 2.5 ppm elemental concentrations of Mg. These procedures were performed in the CIC at the University of Granada.

Through the KPgB interval, large shifts in carbonate content occur, impacting most element distributions. To study elemental variability without this carbonate dilution effect, Al-normalized concentrations or recalculation on a carbonate-free basis is usually applied (Calvert and Pedersen, 1993; De Lange et al., 1987; Morford and Emerson, 1999; Tribovillard et al., 2006; Van der Weijden, 2002). We have selected the following ratios Ca/Al, K/Al, Mg/Al, Cr/Al, Ni/Al, Cu/Al, Zn/Al, Rb/Al, Zr/Al, U/Al, and Mo/Al.

3.2.2. Stable carbon isotope analyses

Stable carbon isotope analyses were performed on 20 samples distributed along the ~32 cm-thick section. Samples were powdered using a Pulverissete 5 agate mill. The $\delta^{13}C$ values of carbonates ($\delta^{13}C_{carb}$) were determined by treatment with phosphoric acid (H_3PO_4 at 103%) using a VG Isocarb system thermostatized at 90 °C. The liberated CO_2 was analyzed with an Isotope Ratio Mass Spectrometer (IRMS) VG Prism II at the University Complutense of Madrid (Spain).

For determination of organic matter $\delta^{13}C$ values ($\delta^{13}C_{org}$), samples were treated with hydrogen chloride (HCl at 3%) for 24 h to remove carbonates and then analyzed with an elemental analyzer Carlo Erba 1108 coupled to a IRMS VG Isochrom in continuous flow mode in the Stable Isotope Laboratory (SIDI) at the Universidad Autónoma of Madrid (Spain). The results were calibrated to the Vienna-Pee Dee Belemnite (V-PDB) standard, with a precision better than 0.1‰. Results are expressed in the common δ-notation in per mil (‰) relative to the V-PDB standard. The reference material used for $\delta^{13}C$ analysis was IA-R001 [$\delta\ ^{13}C_{V\text{-}PDB}$ -26.43‰]. Replicate analysis of samples indicated an average standard deviation of 0.08‰. The international carbonate standard NBS-19 (National Bureau of Standards; $\delta^{13}C = 1.95$‰ and $\delta^{18}O = -2.20$‰) was used to calibrate to V-PDB, with an average precision of 0.1‰ for $\delta^{13}C_{carb}$ and 0.15‰ for $\delta^{13}C_{org}$ analyses.

3.3. Organic geochemistry

3.3.1. Total organic carbon (TOC) analysis

20 samples were selected for determination of total organic carbon (TOC) contents. The analyses were performed in the Analytical Service of the Instituto de Recursos Naturales (IRNAS-CSIC) in Sevilla (Spain) using a SHIMADZU TOC-VCSH. TOC concentration was determined by subtracting the inorganic carbon (IC) from the total carbon (TC) content in each sample.

3.3.2. Biomarker analysis

Organic geochemical analyses were performed in the Department of Geology and the Centro de Instrumentación Científica-Técnica (CICT) at the University of Jaén (Spain). The 16 samples were regularly distributed along the ~32 cm-thick core (equivalent to a stratigraphic length resolution of 2 cm). First, all samples were washed with dichloromethane (DCM) to remove contamination from handling and then crushed using a Pulverissete 5 agate mill. To minimize laboratory contamination, all glassware, aluminum foil, silica, and glass wool were combusted at 550 °C for eight hours and additionally, glassware and metal tools used to process samples were rinsed first with dichloromethane (DCM). Blanks confirmed that there was no laboratory contamination. We recognize that previous work has highlighted the potential contamination risks associated with sample collection (Sosa-Montes de Oca, 2018, Sosa-Montes de Oca et al., 2018a); although we cannot exclude that, we consider it unlikely given the not use of drilling fluids associated with obtaining this short core from outcrop.

About 12 g of dry sediment were extracted using an Accelerated Solvent Extractor (ASE) DIONEX 350 using a solvent mixture of dichloromethane:methanol (DCM:MeOH) (v/v, 4:1) at 100 °C and 7.6×10^6 Pa. We included one blank for every 5 samples. After extraction, the solvent volume was reduced under pressure using a Syncore Polyvap Buchi with a Vacuum Controller V-855 and a Vacuum Pump-V700 at 60 mbar, 30 °C and 70 rpm during 40 min approx.

Activated copper turnings were added to the total lipid extract (TLE) and stirred overnight to remove elemental sulphur from the samples. The Cu turnings were removed, and the TLE was separated using flash column chromatography, using activated alumina as stationary phase, via sequential elution with *n*-hexane (*n*-Hex; 14 ml, yielding saturated hydrocarbons), *n*-Hex:DCM (v/v, 9:1, 14 ml, yielding aromatic compounds), and MeOH (14 ml, yielding polar compounds).

An internal standard, 2.5 μg/ml of androstane, was added to the saturated hydrocarbon fractions prior to analysis by gas chromatography–mass spectrometry (GC–MS). Analyses were carried out on a Thermo Trace Ultra gas chromatograph connected to a Thermo DSQ II mass spectrometer (GC–MS). The GC was fitted with a fused silica capillary column (Supelco Equity–5; 30 m × 0.25 mm × 0.25 μm) and was operated with helium as carrier gas. The samples (in 50 μl Hex) were injected at 70 °C and the oven was subsequently programmed to 130 °C at 20 °C per min and then at 4 °C per min to 300 °C where it was held for 25 min. Biomarkers were identified by comparison of mass spectra and retention time with those reported in the literature (i.e. Peters et al., 2005) and with data from other studies performed in the same equipment (i.e. Quijano et al., 2012); for the identification of gammacerane an authentic standard purchased by Chiron was co–injected.

4. Results

4.1. Major and trace elemental composition

Geochemical data analyzed by ICP-OES and ICP-MS (ICP-OES/MS)

Table 1
Elemental content (major and trace) and elemental ratios, measured by ICP-OES and ICP-MS across the ~32 cm-thick interval in the KPgB at Agost section.

Samples		Distance KPgB	Unit	Major elements				Geochemical proxies												
				(%)				(–)				(x10^{-4})								
Reference Lab.	(g)	(cm)		Mg^{12}	Al^{13}	K^{19}	Ca^{20}	$CaCO_3$*	Mg/Al	Ca/Al	K/Al	Rb/Al	Zr/Al	Cr/Al	Ni/Al	Cu/Al	Zn/Al	Mo/Al	U/Al
22	Ag3 MI 30–32	3.80	20.0		Unit d	0.6	2.5	0.8	26.0	64.9	0.3	10.4	0.3	4.8	8.9	19.2	13.5	4.8	15.6	0.3	0.59
21	Ag3 MI 28–30	3.90	18.0			0.5	2.0	0.7	23.3	58.3	0.3	11.7	0.4	5.4	10.6	22.1	15.6	5.4	17.9	0.3	0.7
20	Ag3 MI 26–28	3.85	16.0			0.6	2.2	0.8	27.2	68.0	0.3	12.4	0.4	4.9	9.1	19.6	14.3	4.9	16.2	0.2	0.7
19	Ag3 MI 24–26	3.95	14.0			0.5	1.9	0.9	28.4	71.1	0.3	14.9	0.5	4.7	8.9	19.3	14.4	4.9	16.5	0.3	0.7
18	Ag3 MI 22–24	3.68	12.0			0.5	1.8	0.8	27.7	69.4	0.3	15.6	0.5	5.4	10.1	19.0	15.9	5.1	16.5	0.3	0.8
17	Ag3 MI 20–22	3.90	10.0			0.6	1.8	0.9	28.8	72.0	0.3	16.4	0.5	5.1	9.5	17.2	14.6	4.4	15.0	0.2	0.8
16	Ag3 MI 18–20	3.80	8.0			0.5	1.7	0.8	28.8	71.9	0.3	17.3	0.5	5.2	10.7	17.0	14.4	4.3	13.9	0.1	0.9
15	Ag3 MI 16–18	3.88	6.0			0.5	1.6	0.8	28.7	71.8	0.3	17.8	0.5	5.3	9.6	16.7	14.9	4.9	15.8	0.1	1.0
14	Ag3 MI 15–16	3.80	4.5		Unit c	0.5	1.7	0.8	28.1	70.3	0.3	16.5	0.5	5.1	9.7	16.5	14.5	5.0	15.3	0.2	1.0
13	Ag3 MI 14–15	3.79	3.5			0.5	1.9	0.8	27.9	69.7	0.3	15.0	0.4	5.3	10.5	16.8	13.7	5.4	14.3	0.2	1.0
12	Ag3 MI 13–14	3.27	2.5			0.5	2.1	0.9	27.4	68.5	0.3	13.1	0.4	5.4	10.3	16.5	12.7	5.2	15.4	0.1	1.0
11	Ag3 MI 12–13	3.14	1.5			0.6	2.1	1.0	26.7	66.7	0.3	12.6	0.5	5.0	9.0	15.0	11.2	4.4	13.2	0.2	0.8
10	Ag3 MI 10–12 Pg	2.23	0.5			0.5	2.0	0.9	28.5	71.2	0.3	14.6	0.5	5.8	9.7	17.2	11.6	5.5	13.8	0.1	0.9
9	K/Pg (10–12)	0.41	0.0		Unit b	0.5	1.8	0.8	28.2	70.5	0.3	15.3	0.5	6.0	10.0	18.5	12.8	6.0	14.7	0.1	1.0
8	K/Pg (8–9)	0.07	0.0			0.4	1.5	1.1	27.6	69.1	0.3	18.5	0.7	10.8	13.6	25.0	17.6	7.2	19.0	0.2	1.4
7	Ag3 MI 10–12 K	2.87	−0.5		Unit a	0.6	1.9	0.9	28.7	71.7	0.3	14.9	0.5	5.5	7.4	16.2	8.9	4.9	12.9	0.1	0.9
6	Ag3 MI 9–10	3.50	−1.5			0.5	1.5	0.8	30.0	75.1	0.3	19.4	0.6	5.3	9.9	16.5	13.2	4.9	12.4	0.1	1.0
5	Ag3 MI 8–9	3.41	−2.5			0.5	1.7	0.7	30.3	75.7	0.3	18.3	0.4	5.3	9.4	16.6	13.0	5.2	14.8	0.2	1.0
4	Ag3 MI 6–8	3.97	−4.0			0.5	1.6	0.9	30.9	77.2	0.3	19.3	0.6	5.0	9.0	15.3	13.5	5.2	15.2	0.1	0.9
3	Ag3 MI 4–6	3.82	−6.0			0.5	1.5	0.9	30.8	77.0	0.3	19.9	0.6	5.7	9.9	16.5	14.6	5.8	15.4	0.1	1.1
2	Ag3 MI 2–4	3.78	−8.0			0.5	1.3	0.8	29.2	73.1	0.4	22.8	0.6	5.5	8.8	16.2	13.7	6.3	15.5	0.2	1.1
1	Ag3 MI 0–2	3.90	−10.0			0.5	1.7	0.9	31.4	78.4	0.3	18.6	0.5	7.9	13.6	22.0	18.2	6.9	21.8	0.2	1.3

* Calculated from Ca*2.5.

are presented as elemental ratios (Ca/Al, K/Al, Mg/Al, Cr/Al, Ni/Al, Cu/Al, Zn/Al, Rb/Al, Zr/Al, U/Al and Mo/Al) across the KPgB and shown in Table 1 and Fig. 2. Selected Al-normalized ratios provide information about environmental variations at continuous, cm-resolution along the ~32 cm-thick studied interval. Elemental ratios related to the meteorite input, such as Cr/Al, Ni/Al, Cu/Al and Zn/Al, all clearly identify the ejecta layer (Fig. 2). Some geochemical ratios used as redox indicators, such as Mo/Al and U/Al (Algeo and Tribovillard, 2009; Tribovillard et al., 2012; Zhou et al., 2012) also peak in the ejecta layer, but exhibit complex and contrasting profiles through the rest of the section. In contrast, the Ca/Al ratio and $CaCO_3$ content decrease within the ejecta layer, with values of 15.3 for the Ca/Al ratio and 69.1% for the $CaCO_3$ content (Fig. 2). Typical detrital input ratios, K/Al, Mg/Al, Rb/Al, and Zr/Al, have more complex profiles, with several peaks in the Maastrichtian but also at the ejecta layer, and some variations occurring in the lower Danian, with relatively stable and low values above the boundary clay interval, at 6 cm above the KPgB.

4.2. Stable carbon isotopes

The $\delta^{13}C_{carb}$ profile shows some variability along the section, with values ranging between 1.2 and 1.7‰ (Table 2 and Fig. 3). A $\delta^{13}C_{carb}$ excursion is recorded at the KPgB, with a negative shift of 0.5‰, and a later recovery at ca. 5 cm above the KPgB. The $\delta^{13}C_{org}$ values range between −24.3 and − 26.2‰ and in the upper part of the section have a similar trend to the $\delta^{13}C_{carb}$ curve (Table 2 and Fig. 3); however, they exhibit a positive rather than negative carbon isotope excursion in the clay boundary layer above KPgB.

4.3. TOC content

The TOC content varies from 0.001 to 1.3% along the section (Table 2, Figs. 3, 4). However, most of the values are low and the variability largely arises from three relatively high TOC peaks that occur: at 8 cm below the KPgB in the unit a, gray calcareous marlstone from the uppermost Maastrichtian (0.6%), and at 6 cm and 20 cm above the KPgB, both in the unit d, light marly limestone from the lowermost Danian (0.25 and 1.3%, respectively).

4.4. Biomarkers

The saturated hydrocarbon fractions are dominated by *n*-alkanes (with varying distributions), the acyclic isoprenoids pristane and phytane, and low abundances of steranes and hopanes, of likely eukaryotic and bacterial origin, respectively (Peters et al., 2005).

4.4.1. n-Alkanes

The *n*-alkanes vary in abundance between 3 and 120 μg/g dry weight (hereafter DW) (Fig. 5). The carbon number ranges from 16 to 40, but the distribution and dominant components vary significantly (Table 3a). Long-chain *n*-alkanes (up to $>C_{34}$) occur in all samples (except in one at 1.5 cm below the ejecta layer), but the dominant homologue varies, such that the average chain length (ACL) (Poynter and Eglinton, 1990) varies from 30 to 32 (Table 3a and Fig. 7). This is driven primarily by changes in the proportion of C_{29} vs C_{31} *n*-alkanes, such that the n-$C_{31}/[n\text{-}C_{29} + n\text{-}C_{31}]$ ratio (Schefuß et al., 2003) exhibits similar variations as the ACL through the section (Table 3a and Fig. 7).

Short-chain *n*-alkanes (C_{17}-C_{19}) are absent or occur in low abundances throughout the section (Fig. 5), despite the thermal maturity of the sediments (see below). The lack of short-chain and predominance of long-chain *n*-alkanes suggests that the organic matter has a significant terrigenous source. To evaluate that further, we calculated the high-molecular-weight (HMW) *n*-alkanes vs ∑total *n*-alkanes ratio ($[n\text{-}C_{25} + n\text{-}C_{26} + n\text{-}C_{27} + n\text{-}C_{28} + n\text{-}C_{29} + n\text{-}C_{30} + n\text{-}C_{31} + n\text{-}C_{32} + n\text{-}C_{33} + n\text{-}C_{34} + n\text{-}C_{35} + n\text{-}C_{36} + n\text{-}C_{37} + n\text{-}C_{38} + n\text{-}C_{40}]/[\sum$ total *n*-alkanes]) (Fig. 5). Values are generally high, exceeding 0.7, but are particularly high in the

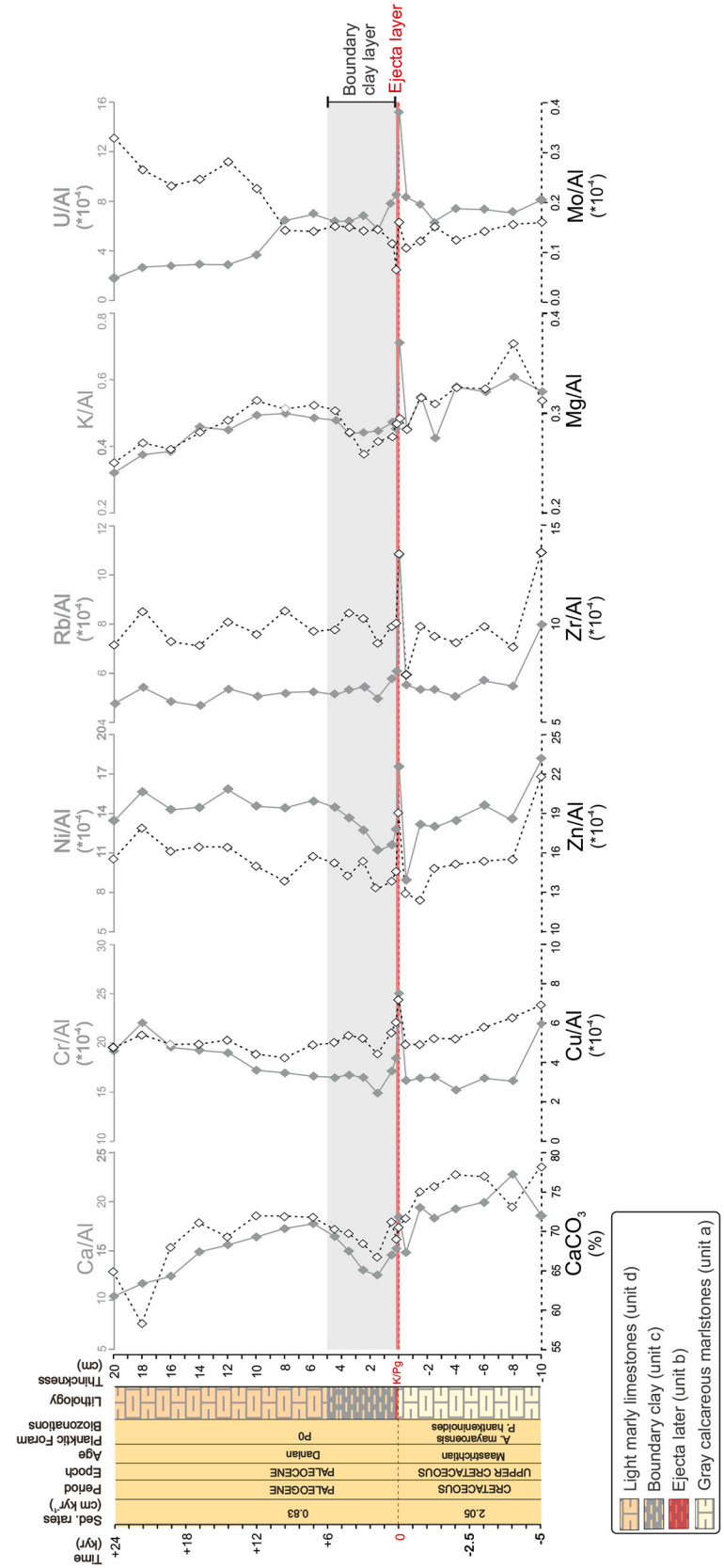

Fig. 2. Elemental/Al (x 10^{-4}) profiles from the KPgB at Agost section. Cr/Al, Ni/Al, Cu/Al, Zn/Al ratios are related to the meteorite input; Mo/Al and U/Al ratios are used as redox proxies; and K/Al, Mg/Al, Rb/Al, and Zr/Al ratios are related to detrital input. Top geochemical ratios are represented by continuous lines and bottom geochemical ratios by dashed lines. Lithologically, from the bottom to the top: (unit a) gray calcareous marlstones and marlstones from the late Maastrichtian (Cretaceous) and the three overlying Paleogene units from the early Danian: (unit b) a 2–3 mm-thick red clay (the ejecta layer), (unit c) blackish-gray clay layer (the boundary clay), and (unit d) light marly limestones. Planktic foraminiferal zones are based on Molina et al. (2005), while magnetostratigraphy is based on Groot et al. (1989). (For interpretation of the references to colour in this figure legend, the reader is referred to the web version of this article.)

Table 2
Total organic carbon content (TOC, %) and stable carbon isotopic composition (‰ V-PDV) across the KPgB at Agost section.

Samples*		Distance KPgB	Unit	$C_{inorganic}$	$C_{organic}$ (TOC)	C_{total}	Stable carbon isotopes	
		(cm)		(%)	(%)	(%)	$\delta^{13}C_{org}$	$\delta^{13}C_{carb}$
22	Ag3 MI 30–32	20.0	Unit d	7.7	1.3	9.0	−25.6	1.5
21	Ag3 MI 28–30	18.0		9.5	0.0	9.5	−25.4	1.7
20	Ag3 MI 26–28	16.0		8.8	0.1	8.9	−25.6	1.7
19	Ag3 MI 24–26	14.0		9.6	0.0	9.6	−25.7	1.5
18	Ag3 MI 22–24	12.0		9.2	0.0	9.2	−25.0	1.6
17	Ag3 MI 20–22	10.0		9.6	0.0	9.6	−25.5	1.5
16	Ag3 MI 18–20	8.0		9.6	0.0	9.6	−24.6	1.7
15	Ag3 MI 16–18	6.0		9.2	0.3	9.5	−25.0	1.7
14	Ag3 MI 15–16	4.5	Unit c	9.7	0.0	9.7	−24.3	1.7
13	Ag3 MI 14–15	3.5		8.1	0.0	8.1	−24.5	1.5
12	Ag3 MI 13–14	2.5		9.0	0.0	9.0	−24.7	1.4
11	Ag3 MI 12–13	1.5		8.7	0.1	8.8	−24.8	1.3
10	Ag3 MI 10–12 Pg	0.5		9.3	0.1	9.4	−24.6	1.2
7	Ag3 MI 10–12 K	−0.5	Unit a	9.1	0.0	9.1	−24.7	1.7
6	Ag3 MI 9–10	−1.5		9.5	0.0	9.5	−25.0	1.6
5	Ag3 MI 8–9	−2.5		9.8	0.0	9.8	−25.2	1.5
4	Ag3 MI 6–8	−4.0		9.8	0.0	9.8	−25.3	1.7
3	Ag3 MI 4–6	−6.0		9.8	0.0	9.9	−25.2	1.4
2	Ag3 MI 2–4	−8.0		9.1	0.6	9.7	−24.7	1.6
1	Ag3 MI 0–2	−10.0		9.7	0.0	9.7	−26.2	1.5

* The ejecta layer was not analyzed because there was not enough sample material.

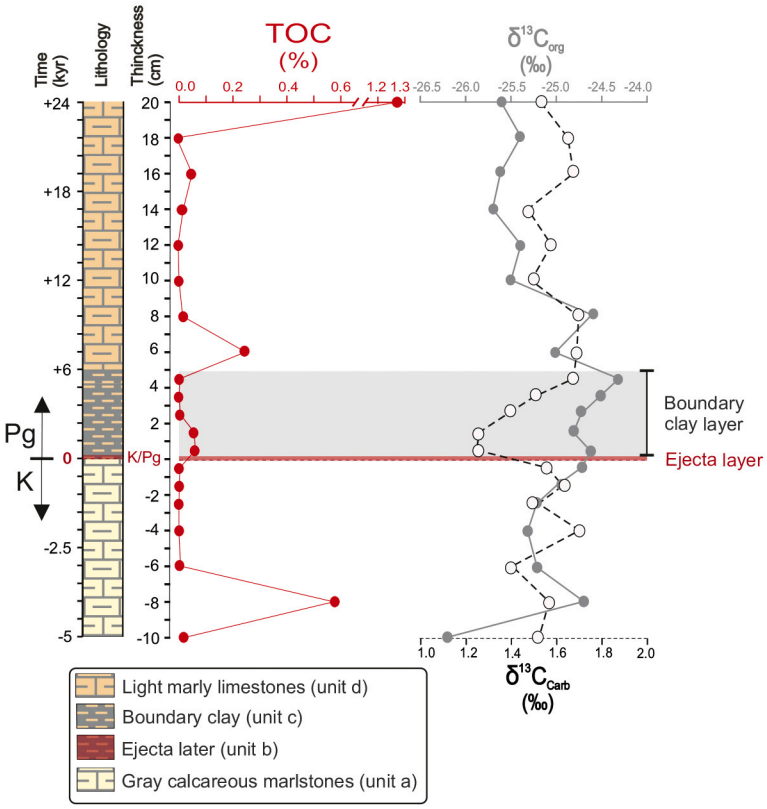

Fig. 3. Total organic carbon content (TOC, %) and stable carbon isotopes profiles (‰ V-PDB) from the KPgB at Agost section. $\delta^{13}C_{org}$ is represented by continuous line and $\delta^{13}C_{carb}$ by dashed line. For lithology, see caption in Fig. 2.

interval after the KPgB (unit c), which supports a predominant terrigenous source of OM in this interval.

To facilitate the interpretation of *n*-alkane distributions in relation to the source, diagenetic alteration and thermal maturity, we have also calculated the Carbon Preference Index ($CPI = 1/2*\Sigma(X_i + X_{i+2} + \ldots + X_n)/\Sigma(X_{i-1} + X_{i+1} + .. + X_{n-1}) + 0.5*\Sigma(X_i + X_{i+2} + \ldots + X_n)/\Sigma(X_{i+1} + X_{i+3} + \ldots + X_{n+1})$, with $i = 25$ and $n = 35$) (Bray and Evans, 1961; Peters et al., 2005) (Table 3a and Fig. 6). CPIs are typically high in leaf waxes (>5; e.g. Eglinton and Hamilton, 1963; Mazurek and Simoneit, 1984), decrease in soils and sediments to values between 2 and 5 (Kennicutt et al., 1987) due to diagenetic alteration, and approach 1 in thermally mature rocks (e.g. Gearing et al., 1976; Pendoley, 1992). Here, CPIs are all slightly above 1 and vary through the section (Fig. 6). However, they are particularly variable in the gray calcareous marlstones (unit a), and in the boundary clay layer (unit c) from the lowermost Danian, with values as high as 1.6, confirming at least a partial higher plant origin. In

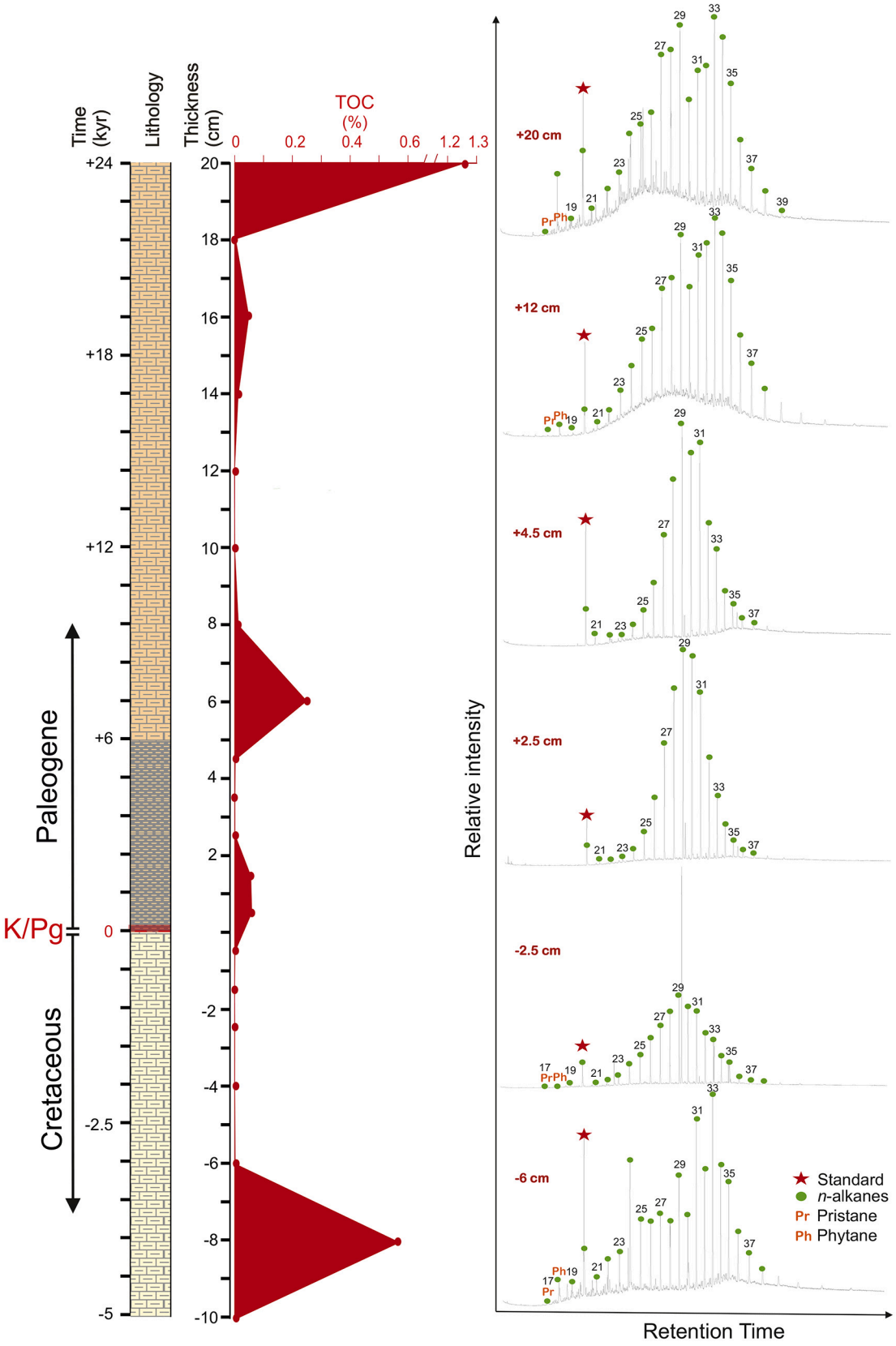

Fig. 4. Total organic carbon (TOC, %) profile from the KPgB at Agost section alongside six partial gas chromatograms derived from GC–MS total ion currents (TIC); the selected traces are representative of units a, c and d described above, with the main biomarkers identified. For lithology, see caption in Fig. 2.

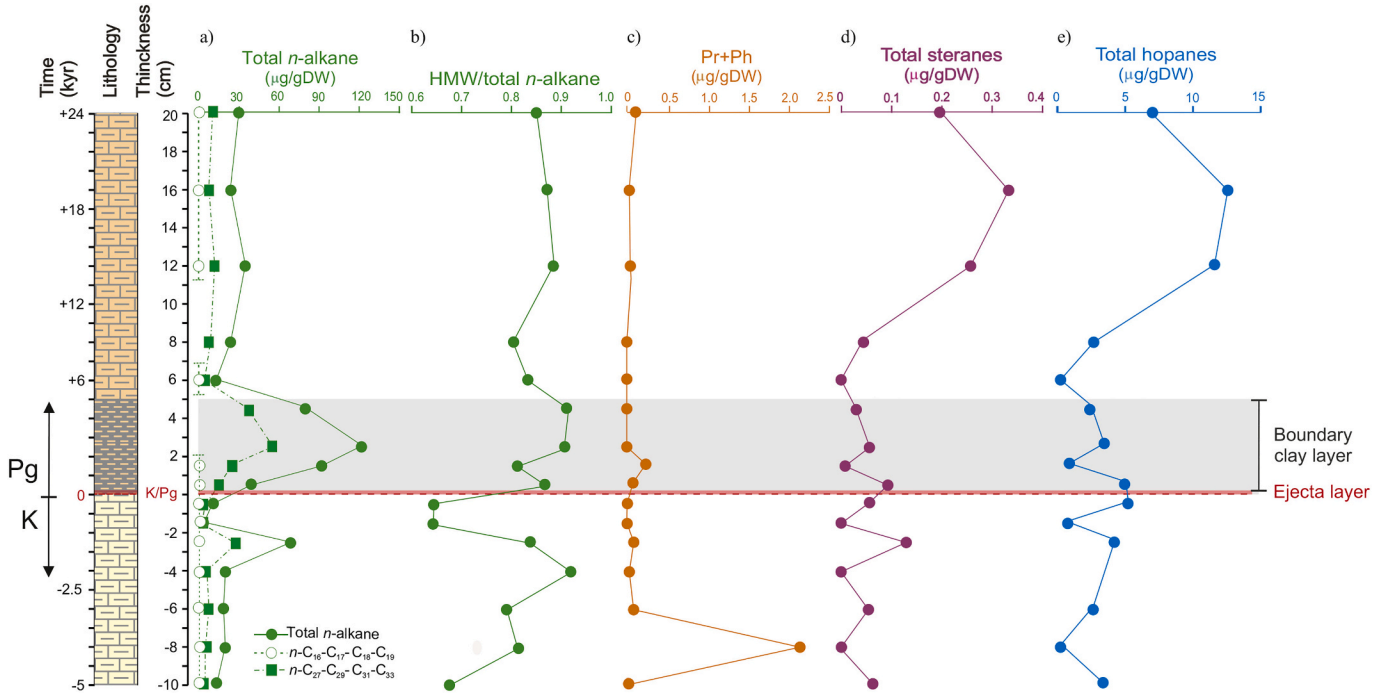

Fig. 5. Abundances of main biomarkers through the KPgB at Agost section. Concentration in µg/g dry weight (DW) of a) total *n*-alkane [Σ(*n*-C_{16} + … + *n*-C_{40})], b) HMW/∑total *n*-alkane ratio [Σ (*n*-C_{27} + … + *n*-C_{40}) / Σ(*n*-C_{16} + … + *n*-C_{40})] (green colour), c) acyclic isoprenoids concentration, (Pr + Ph; orange colour), d) total sterane concentration [Σ(C_{27} + C_{28} + C_{29})] (pink colour), and e) total hopane concentrations [Σ (C_{27} + … + C_{35})] (blue colour). For lithology details see caption in Fig. 2. (For interpretation of the references to colour in this figure legend, the reader is referred to the web version of this article.)

Table 3a
Main *n*-alkanes and acyclic isoprenoids ratios across the KPgB at Agost section. Acyclic isoprenoids concentration, (Pr + Ph) is in µg/g dry weight (DW).

Samples		Distance KPgB	Unit	*n*-alkanes						Acyclic isoprenoids		
		(cm)		Range[a]	C_{max}[b]	ACL[c]	31/(29 + 31)[d]	HMW/∑total *n*-alkane[e]	CPI[f]	Pr/*n*-C_{17}	Ph/*n*-C_{18}	Pr + Ph
22	Ag3 MI 30–32	20.0	Unit d	16–38	33	31	0.42	0.81	1.31	0.27	0.47	0.13
20	Ag3 MI 26–28	16.0		16–40	33	31	0.49	0.84	1.28	0.15	0.35	0.04
18	Ag3 MI 22–24	12.0		17–39	33	31	0.48	0.86	1.25	0.25	0.58	0.06
16	Ag3 MI 18–20	8.0		20–38	31	30	0.53	0.76	1.27	–	–	–
15	Ag3 MI 16–18	6.0		19–37	34	31	0.57	0.79	1.14	–	–	–
14	Ag3 MI 15–16	4.5	Unit c	20–37	29	30	0.47	0.89	1.15	–	–	–
12	Ag3 MI 13–14	2.5		20–37	29	30	0.42	0.89	1.07	–	–	–
11	Ag3 MI 12–13	1.5		18–40	33	31	0.56	0.76	1.48	–	0.29	0.23
10	Ag3 MI 10–12 Pg	0.5		17–38	33	31	0.51	0.84	1.18	0.20	0.57	0.10
7	Ag3 MI 10–12 K	−0.5	Unit a	17–37	31	30	0.53	0.55	1.56	0.19	0.41	0.02
6	Ag3 MI 9–10	−1.5		17–34	24	30	0.56	0.56	1.39	0.53	0.26	0.03
5	Ag3 MI 8–9	−2.5		17–38	29	30	0.47	0.80	1.15	0.34	0.40	0.12
4	Ag3 MI 6–8	−4.0		18–39	34	32	0.60	0.90	1.22	–	2.85	0.05
3	Ag3 MI 4–6	−6.0		17–38	33	31	0.59	0.74	1.55	0.43	0.57	0.12
2	Ag3 MI 2–4	−8.0		17–39	34	31	0.58	0.77	1.36	0.98	2.04	2.14
1	Ag3 MI 0–2	−10.0		18–39	33	30	0.59	0.60	1.29	–	0.27	0.02

[a] The detected carbon number range of *n*-alkanes.
[b] Carbon number of the homologue with highest abundance.
[c] Average chain length ACL = Σ(i*X_i)/ΣX_i, where X is abundance and i ranges from C_{25} to C_{35}.
[d] Ratio of the *n*-C_{31} to the sum of the *n*-C_{29} and *n*-C_{31} alkane.
[e] HMW/∑total *n*-alkanes = Σ(C_{27} + … + C_{40}/ΣC_{16} + … + C_{40}). [f] Carbon Preference Index CPI = 1/2*Σ(X_i + X_{i+2} + .. + X_n)/Σ(X_{i-1} + X_{i+1} + .. + X_{n-1}) + 0.5*Σ(X_i + X_{i+2} + .. + X_n)/Σ(X_{i+1} + X_{i+3} + … + X_{n+1}), with i = 25 and *n* = 35.

the Danian, from 8 cm above the KPgB and within the light marly limestones (unit d), CPIs have stable and low values of ~1.3.

4.4.2. *Acyclic isoprenoids*

The acyclic isoprenoids, pristane (Pr) and phytane (Ph), derive from multiple sources but in this setting, most likely from aquatic phytoplankton via the degradation of the phytyl side-chain of chlorophyll (Peters et al., 2005). Their abundances vary dramatically but non-systematically through the section, with some intervals where they are absent or below detection limits (Table 3a). Maximum abundances (µg/g DW) of summed Pr + Ph occur at 8 and 2.5 cm below and at 1.5 cm above the KPgB, respectively (Fig. 5); lowest abundances generally occur above the KPgB, with neither compound found between 1.5 and 12 cm. The Pr/*n*-C_{17} ratios range between 0 and 1.5, and the Ph/*n*-C_{18} ratios range between 0.3 and 2.9, with highest values generally in unit a (Fig. 7). These variations largely reflect the variations in *n*-alkane abundances (see above). The overall low abundances of these acyclic isoprenoids could be consistent with a predominantly terrigenous source

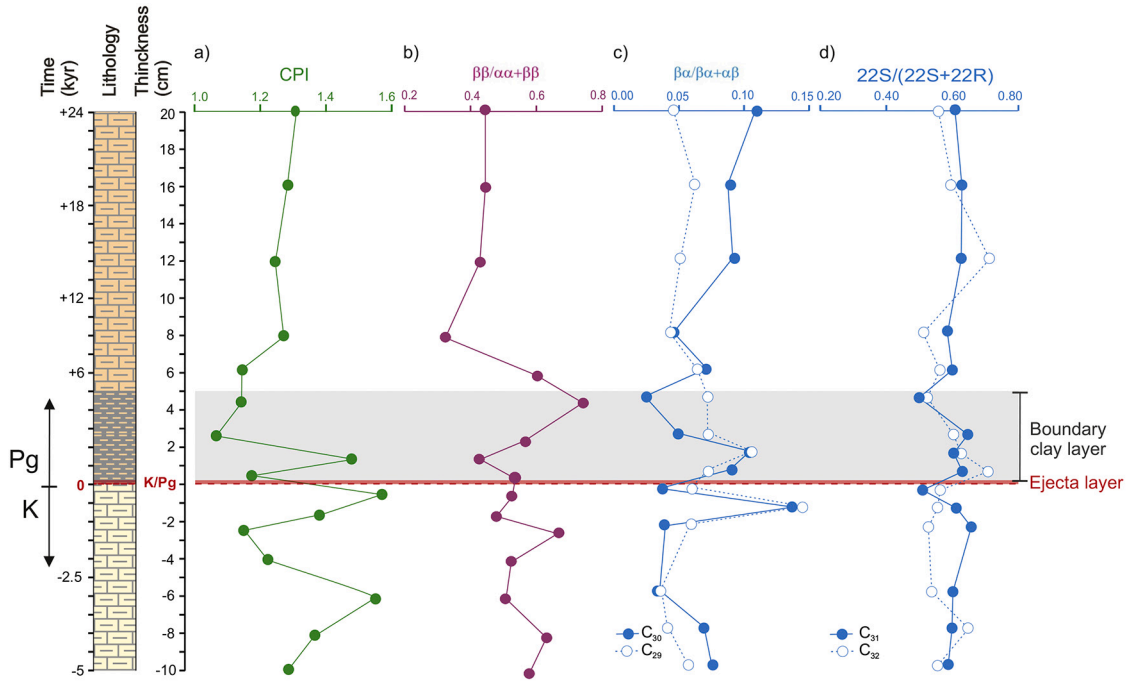

Fig. 6. Biomarker ratios indicative of thermal maturity or other chemical alteration. a) CPI from *n*-alkane [1/2*Σ(X_i + X_{i+2} + … + X_n)/Σ(X_{i-1} + X_{i+1} + .. + X_{n-1}) + 0.5*Σ(X_i + X_{i+2} + … + X_n)/Σ(X_{i+1} + X_{i+3} + … + X_{n+1})], with i = 25 and n = 35) (green colour), b) C_{29} ββ/(αα + ββ) sterane ratio (pink colour), c) C_{31} and C_{32} 22S/(22S + 22R), and d) βα/(βα + αβ) hopane ratios (blue colour). For lithology, see caption in Fig. 2. (For interpretation of the references to colour in this figure legend, the reader is referred to the web version of this article.)

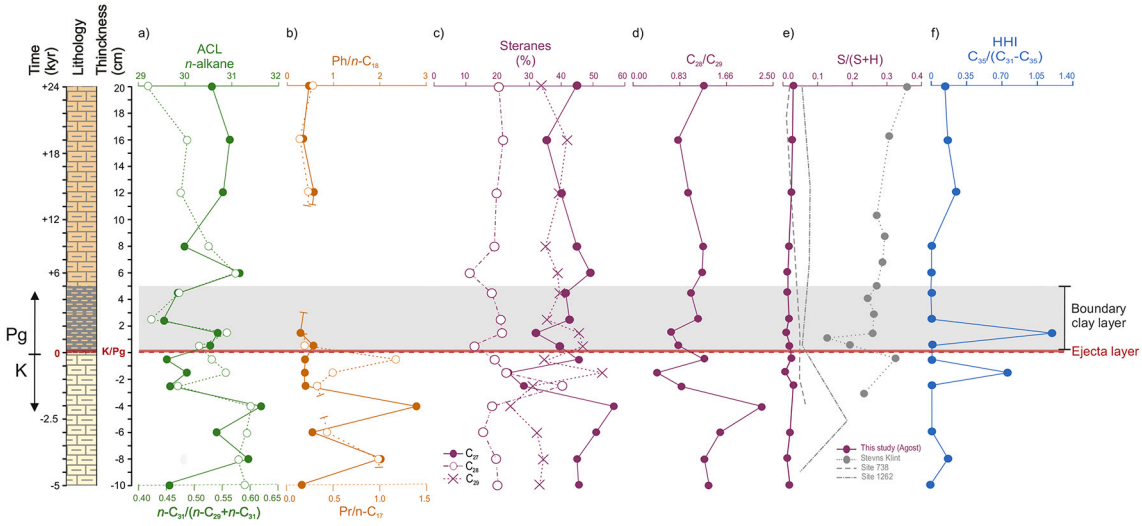

Fig. 7. Biomarker ratios indicative of source changes in the KPgB at Agost section.
a) ACL (Average Chain Length) from *n*-alkane [Σ(i*X_i)/ΣX_i] where X is abundance and i ranges from C_{25} to C_{35} (continuous green line) and *n*-C_{31}/[*n*-C_{29} + *n*-C_{31}] ratio (dashed green line), b) Pr/*n*-C_{17} (dashed orange line) and Ph/*n*-C_{18} (continuous orange line) ratios, c) % of each regular sterane [C_{27}/ Σ(C_{27} + C_{28} + C_{29}); C_{28}/Σ(C_{27} + C_{28} + C_{29}); C_{29}/ Σ(C_{27} + C_{28} + C_{29})], d) C_{28}/C_{29} sterane ratio, e) sterane/hopane ratio (S/S + H) [Σ (C_{27} + C_{28} + C_{29}) / (C_{27} + C_{28} + C_{29}) + (ΣC_{27} + … + C_{35})], pink colour for the Agost section and gray colours for Stevn Klint section (data from Sepúlveda et al., 2009) and sites 738 and 1262 (data from Bralower et al., 2020), and f) Homohopane indices (HHI) [C_{35}/(C_{31}-C_{35})] (blue colour). For lithology, see caption in Fig. 2. (For interpretation of the references to colour in this figure legend, the reader is referred to the web version of this article.)

of the organic matter throughout the section and preclude the use of classical redox proxies based on the Pr/Ph ratio (Didyk et al., 1978; Ten Haven et al., 1987).

4.4.3. Steranes

Steranes (C_{27}-C_{29}) are tetracyclic triterpanes arising from diagenetic alteration of sterols and consequently derive almost exclusively from eukaryotic organisms (e.g. Peters et al., 2005; Schwark and Empt, 2006 and references therein), particularly marine phytoplankton (Volkman et al., 1998). The predominant three regular steranes, C_{27}-cholestane, C_{28}-ergostane and C_{29}-stigmastane, are present in all samples but in highly variable concentrations (Table 3b and Fig. 5). They are represented by the four epimers (5α(H),14α(H),17α(H),20R; 5α(H),14α(H),17α(H),20S; 5α(H),14β(H),17β(H),20S and 5α(H),14β(H),17β

Table 3b
Sterane ratios across the KPgB interval at Agost section.

Samples		Distance KPgB	Unit	Steranes							
				Range[a]	C_{max}[b]	Presence of Diasterane	C_{28}/C_{29}	S/(S + H)[c]		C_{27}-C_{29}	C_{27}-C_{29}
		(cm)							*n*-alkane/S[d]	ββ/αα + ββ	20S/20S + 20R
22	Ag3 MI 30–32	20.0	Unit d	27–29	27	Yes	1.33	0.03	153.74	1.3	1.5
20	Ag3 MI 26–28	16.0		27–29	29	Yes	0.85	0.03	74.61	1.4	1.5
18	Ag3 MI 22–24	12.0		27–29	27	Yes	1.02	0.02	135.94	1.5	1.6
16	Ag3 MI 18–20	8.0		27–29	27	Yes	1.28	0.02	532.73	1.1	1.3
15	Ag3 MI 16–18	6.0		27–29	27	Yes	1.26	0.01	2989.63	1.5	1.0
14	Ag3 MI 15–16	4.5	Unit c	27–29	27	Yes	1.05	0.01	2588.11	1.4	1.3
12	Ag3 MI 13–14	2.5		27–29	27	Yes	1.20	0.02	2113.63	1.2	1.3
11	Ag3 MI 12–13	1.5		27–29	29	Yes	0.71	0.01	9190.13	1.3	1.5
10	Ag3 MI 10–12 Pg	0.5		27–29	29	Yes	0.85	0.02	427.31	1.3	1.3
7	Ag3 MI 10–12 K	−0.5	Unit a	27–29	27	Yes	1.30	0.02	92.05	1.3	1.5
6	Ag3 MI 9–10	−1.5		27–29	29	Yes	0.45	0.01	451.18	1.3	1.5
5	Ag3 MI 8–9	−2.5		27–29	28	Yes	0.90	0.03	535.86	1.4	0.8
4	Ag3 MI 6–8	−4.0		27–29	27	Yes	2.33	–	12,217.35	1.6	1.2
3	Ag3 MI 4–6	−6.0		27–29	27	Yes	1.57	0.02	331.18	1.3	1.4
2	Ag3 MI 2–4	−8.0		27–29	27	Yes	1.31	0.01	6000.75	1.5	1.0
1	Ag3 MI 0–2	−10.0		27–29	27	Yes	1.36	0.02	212.07	1.4	1.3

[a] The detected carbon number range of steranes.
[b] Carbon number with the highest abundance.
[c] The sterane/(sterane + hopane) ratio [(Σ C_{27} + C_{28} + C_{29})/(Σ C_{27} + C_{28} + C_{29}) + (Σ C_{27} + … + C_{35})].
[d] The *n*-alkane ratio/sterane/[(Σ *n*-alkane)/(Σ C_{27} + C_{28} + C_{29})].

(H),20R). The C_{30} regular sterane has also been identified in most of the samples. Also present are the 13β,17α steranes or diasteranes (Table 3b). Collectively, the sterane and diasterane distributions are consistent with a relatively high thermal maturity, near the onset of the oil window (Table 3c).

Regular sterane (C_{27}, C_{28} and C_{29}) distributions vary significantly through the section. The most abundant sterane in most Maastrichtian sediments is the C_{27} component; across the KPgB, at 1.5 cm below the KPgB and between 0.5 and 1.5 cm above it, the C_{29} sterane dominates; in the uppermost part of the section, the C_{27} and C_{29} components occur in similar abundances (Fig. 7). Relative abundances of the C_{28} sterane are more stable, reflected both by its overall proportion as well as invariant C_{28}/C_{29} sterane ratios (barring a value of 2.5 below the KPgB; Fig. 7). Sterane abundances also vary relative to those of bacterially-derived hopanes, such that the sterane/(sterane+hopane) ratio [S/(S + H), i.e. Σ C_{27} + C_{28} + C_{29} steranes/(Σ C_{27} + C_{28} + C_{29} steranes) + (Σ C_{27} + … +

Table 3c
Hopanes ratios across the KPgB interval at Agost section.

Samples		Distance KPgB	Unit	Hopanes									
				Range[a]	Presence of Gammacerane	ACL[b]	Ts/Tm	C_{29}/C_{30}	C_{29} βα/(αβ + βα)	C_{30} βα/(αβ + βα)	C_{31} 22S/(22S + 22R)	C_{32} 22S/(22S + 22R)	HHI[c] C_{35}/(C_{31}-C_{35})
		(cm)											
22	Ag3 MI 30–32	20.0	Unit d	27–35	–	31	0.55	1.27	0.05	0.11	0.55	0.48	0.17
20	Ag3 MI 26–28	16.0		27–35	–	30	0.98	1.32	0.06	0.09	0.58	0.54	0.21
18	Ag3 MI 22–24	12.0		27–35	–	30	0.87	1.32	0.05	0.09	0.58	0.69	0.30
16	Ag3 MI 18–20	8.0		27–33	–	30	1.11	1.11	0.04	0.05	0.52	0.42	0.00
15	Ag3 MI 16–18	6.0		27–33	–	30	1.25	1.39	0.06	0.07	0.54	0.49	0.00
14	Ag3 MI 15–16	4.5	Unit c	27–33	–	30	1.04	1.27	0.07	0.02	0.41	0.44	0.00
12	Ag3 MI 13–14	2.5		27–33	–	30	0.63	1.29	0.07	0.05	0.61	0.55	0.00
11	Ag3 MI 12–13	1.5		27–35	–	31	1.08	0.77	0.11	0.10	0.55	0.58	1.52
10	Ag3 MI 10–12 Pg	0.5		27–34	Yes	30	1.05	1.18	0.07	0.09	0.58	0.69	0.00
7	Ag3 MI 10–12 K	−0.5	Unit a	27–32	Yes	30	1.05	0.98	0.06	0.04	0.42	0.49	0.00
6	Ag3 MI 9–10	−1.5		27–35	–	31	1.28	0.66	0.15	0.14	0.56	0.48	0.76
5	Ag3 MI 8–9	−2.5		27–33	–	30	0.54	0.99	0.06	0.04	0.62	0.44	0.00
4	Ag3 MI 6–8	−4.0		–	–		–	–	–	–	–	–	–
3	Ag3 MI 4–6	−6.0		27–33	–	30	1.59	1.44	0.04	0.04	0.54	0.46	0.00
2	Ag3 MI 2–4	−8.0		27–35	–	31	0.81	1.11	0.04	0.07	0.54	0.61	0.19
1	Ag3 MI 0–2	−10.0		27–33	–	30	1.02	1.13	0.06	0.08	0.52	0.48	0.00

[a] The detected carbon number range of hopanes.
[b] ACL = Σ(i*X_i)/ΣX_i, where X is abundance and i ranges from C_{27} to C_{35}.
[c] The homohopane indices (HHI) [C_{35}/(C_{31}-C_{35})].

C_{35} hopanes)], calculated from the *m/z* 217 and 191 traces, respectively, is low in Maastrichtian sediments, variable across the KPgB and relatively high in the uppermost part of the section (Fig. 7).

Intriguingly, sterane-derived thermal maturity parameters also differ between the lower and upper parts of the section. The C_{29} ββ/(αα + ββ) ratio, which increases with thermal maturity (Mackenzie et al., 1980), is generally higher in the lower part of unit a (Maastrichtian), variable across the boundary layer, high again at the top of unit c (clay boundary layer), and then decreases at the base of unit d to relatively low and stable values of 0.41 upwards (Danian) (Table 3b and Fig. 6). Given the thickness of this section, it is unlikely that these values reflect thermal maturity variations of the rocks themselves; below in the discussion, changes in OM source input are considered as an alternative mechanism.

4.4.4. Hopanes

Hopanes are derived from functionalized bacteriohopanoids that are common in a wide range of predominantly but not exclusively aerobic bacteria (Belin et al., 2018; Rohmer et al., 1984). The hopanes and homohopanes (>C_{30} hopanes) range in carbon number from C_{27} to C_{35} and occur in almost all of the samples across the KPgB (Table 3c and Fig. 5). Hopanes were not detected at 4.0 cm below the KPgB, and C_{34}-C_{35} homohopanes were absent/below detection in about half of the samples (Table 3c). Therefore, homohopane indices (HHI) [C_{35}/(C_{31}-C_{35})], which reflect the increased preservation of extended hopanes (>C_{33}) under anoxic conditions (Bishop and Farrimond, 1995; Peters et al., 2005), are generally very low. However, minor peaks in HHIs do occur just above and below the KPgB (Fig. 7). Intriguingly, the distribution of hopanes varies through the section, such that the <C_{31} hopanes are dominant before the event and >C_{30} hopanes are dominant afterwards (Table 3c). The 17α(H)-22,29,30-trisnorhopanes (Tm) and 18α(H)-22,29,30-trisnorneohopanes (Ts) are present in all samples, with a Ts/Tm ratio ranging between 0.54 and 1.3, with a mean value of 1.1 from the upper Maastrichtian sediments and 0.95 from the lower Danian sediments (Table 3c). Gammacerane (C_{30} triterpane) was identified only in two samples around the ejecta layer, at 0.5 cm below and above the KPgB (Table 3c), but only at low concentrations close to the detection limit.

Several hopane ratios predominantly (but not exclusively) reflect thermal maturity (Mackenzie et al., 1980; Seifert and Moldowan, 1980). The C_{29} and C_{30} 17β,21α(H)/(17β,21α(H) + 17α,21β(H)) hopane ratios –hereafter βα/(βα + αβ) ratios (or moretane/hopane ratio)– largely covary between 0.02 and 0.11 (Table 3c and Fig. 6), and the C_{31} and C_{32} 22S/(22S + 22R) 17α,21β(H)-homohopane ratios range between 0.41 and 0.69 (Table 3c and Fig. 6). Both the low βα/(βα + αβ) hopane ratios and near-equilibrium 22S/(22S + 22R) ratios indicate a relatively high thermal maturity close to oil generation (equivalent vitrinite reflectance at or near 0.6, Peters et al., 2005). This is also consistent with the absence of the ββ hopane configuration. However, there are large variations in all ratios, and especially the βα/(βα + αβ) hopane ratios; as with steranes, this variability is not thought to reflect changes in the thermal history of these rocks.

5. Discussion

The KPgB mass extinction strongly impacted phytoplankton and calcareous nannoplankton (Alvarez et al., 2019; Lowery et al., 2020), but the response of non-fossilizing plankton remains less clear (Lowery et al., 2020). Until now, there are few studies based on biomarkers (Bralower et al., 2020; Schaefer et al., 2020; Sepúlveda et al., 2009; Taylor et al., 2018). Here, we first integrate new biomarker data with some elemental ratios to evaluate changes in environmental conditions. We then use specific biomarkers to characterize changes in the OM assemblages along the continuous 32 cm sequence of the KPgB in the Agost distal section (SE Spain), and compare them to those environmental changes. We further evaluate the relative contribution of terrigenous, algal and bacterial OM as well as reworked OM (the latter inferred from changes in the thermal maturity of the biomarkers). Then we examine hopane and sterane distributions in greater detail, using those to explore the recovery of primary producers, mainly bacterial and algal communities, after the KPgB extinction.

5.1. Changes in environmental conditions

The elemental analysis performed at the Agost section confirms the preservation of the ejecta layer in our study section, defined by a peak in Cr/Al, Ni/Al, Cu/Al, and Zn/Al ratios related to extraterrestrial input. However, the ejecta layer also exhibits peaks in others ratios such as Mo/Al and U/Al, widely considered as proxies for paleoredox conditions (Algeo and Tribovillard, 2009; Tribovillard et al., 2012). These ratios indicate that changes in the oxygen water conditions occurred at the KPg impact (detected only in the ejecta layer), although minor variations in both profiles also occur elsewhere in the section (Fig. 2). In the nearby Caravaca section, Sosa-Montes de Oca et al. (2013) showed that depositional conditions for the ejecta layer were anoxic, inferred to be a consequence of the enhanced contribution of metals to the basins as well as an increased supply of terrestrial and marine organic material. However, shortly after the impact, oxygen levels rapidly recovered, favoring the earliest macrobenthic opportunist colonization (Rodríguez-Tovar, 2005).

At the Agost site, the enrichment factor (EF) of selected trace elements, in particular uranium and molybdenum, which are enriched in anoxic conditions, U_{EF} vs Mo_{EF} (Fig. 8), indicates a change in redox conditions immediately following the KPgB but without anoxic conditions ever being reached (Fig. 8). This is likey due to the Agost section (upper-bathyal) being shallower than the Caravaca section (bathyal) (Schulte et al., 2010). Furthermore, Mo increases from 8 cm onwards above the KPgB, indicating further minor changes in redox conditions. We do not have biomarker data from the thin ejecta layer, but biomarkers in sub- and super-adjacent layers are consistent with this being the interval with the most reducing conditions. Gammacerane, thought to derive from bacteriovorous ciliates and an indicator of anoxia (Peters et al., 2005; Sinninghe-Damste et al., 1995), is present only in rocks 0.5 cm below and above the KPgB (Table 3c). Similarly, the redox sensitive homohopane indices (HHI = [C_{35}/(C_{31}-C_{35})]; Bishop and Farrimond, 1995; Peters et al., 2005) are generally low, but two maxima occur at 2.5 below and 1.5 cm above the KPgB (Fig. 7), also suggesting episodic anoxia or dysoxia in the bottom waters in the latest Cretaceous and early Danian after deposition of the ejecta layer.

5.2. Variability in organic matter input across the KPgB event

The *n*-alkanes primarily drive from leaf waxes of vascular plants, and this is especially the case for the long-chain *n*-alkanes (>C_{25}) with an odd carbon number (e.g. Eglinton and Hamilton, 1967; Eglinton and Eglinton, 2008). However, *n*-alkyl moieties also occur in various macromolecules, including algaenan, cutin, cutan and suberin (e.g. (Gelin et al., 1999, 1998; Tegelaar et al., 1989). Therefore, HMW components in geological materials, especially when the odd-over-predominance has been largely lost, can derive from a range of sources (Eglinton and Eglinton, 2008). Conversely, short-chain *n*-alkanes (C_{15}-C_{19}) are thought to mainly derive from aquatic sources, including algae and photosynthetic bacteria (Cranwell et al., 1987; Gelpi et al., 1970); however, like their long-chain homologues, in thermally mature sediments they also derive from the diagenetic and thermal degradation of a wide range of biological sources. Consequently, because of its high thermal maturity, interpretation of *n*-alkane distributions in Agost sediments is challenging. Nonetheless, the dominance of >C_{23} components (and high HMW/∑total *n*-alkane ratios >0.7) throughout the sequence, as well as very low abundances of Pr and Ph (Fig. 5), suggest that terrigenous inputs were relatively dominant. This could be particularly true in the lower part of the section, Maastrichtian (unit a) and lowermost boundary clay layer (unit c), where an elevated CPI above 1.4 persists in some

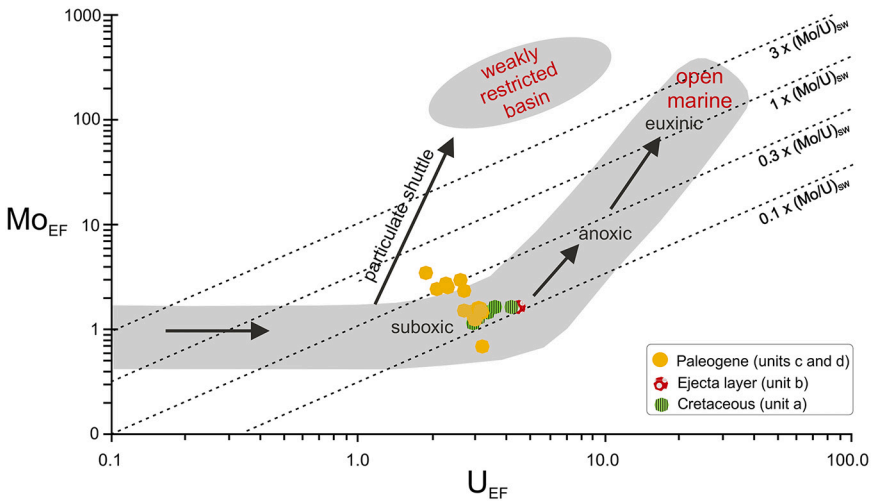

Fig. 8. Mo_{EF} vs U_{EF} covariation for the KPgB at Agost section. The uppermost Maastrichtian sediments (unit a) are indicated by green circles with vertical stripes, the ejecta layer (unit b) is noted by red circles with dots and the lowermost Danian sediments (units c and d) by yellow circles. (For interpretation of the references to colour in this figure legend, the reader is referred to the web version of this article.)

horizons (Fig. 6). The HMW/∑total *n*-alkane ratio, however, does not show similar trends, with higher values mostly associated with the upper part of the section, from 2.5 to 20 cm above the KPgB (Fig. 5). Consequently, it appears that higher plant inputs were variable and complex, and likely overprinted by inputs from more thermally mature sources.

Further evidence for erosive change comes from the unexpected variations in biomarker thermal maturity parameters, especially in a ~ 32 cm-thick section with no differences in burial history. The lower values are likely representative of the history of the basin, whereas higher values could be evidence of reworked allochthonous organic matter (e.g. Carmichael et al., 2018; Castro et al., 2019; Hackley et al., 2020; van Breugel et al., 2007). Thermal maturity parameters are also impacted by lithology (Peters et al., 2005; Peters and Moldowan, 1991), but we discount that explanation given the minor lithological variations in this section and their lack of correspondence with biomarker parameters. In fact, the biomarker maturity parameters exhibit rather inconsistent trends. The sterane ββ/(αα + ββ) ratio is highest in the lower part of the section, but the hopane 22S/(22S + 22R) is lowest in isolated horizons between 2 cm below and 8 cm above the KPgB (Fig. 6). In contrast, the βα/(βα + αβ) hopane ratio, which decreases with thermal maturity, is highest at 1.5 cm below and above the KPgB (Fig. 6). We note, however, that high moretane/hopane ratios are also associated with terrestrial inputs (Xie et al., 2007). Thus, it appears that the interval immediately preceding the KPgB through to the boundary clay layer is characterized by highly variable terrestrial inputs, from both higher plants and reworked organic matter in older sedimentary rocks.

Consequently, the proportion of putative aquatic organic matter inputs also appears to vary through the section. Both Pr/*n*-C_{17} and Ph/*n*-C_{18} ratios are higher and more variable prior to the KPgB than after it, perhaps suggesting decreased marine productivity (Fig. 7). The sterane/hopane ratio [S/(S + H)] exhibits a more complex record, varying in the pre-KPgB horizons, decreasing in the boundary layer and stabilizing at maximum values in the uppermost part of the section (unit d) (Fig. 7).

These changes in the OM assemblage likely impacted the bulk organic matter $\delta^{13}C$ record. Negative carbon isotope excursions (-CIEs) in both $\delta^{13}C_{carb}$ and $\delta^{13}C_{org}$ are typical in immediate post-KPgB intervals (Birch et al., 2016; Sepúlveda et al., 2019). Generally, at those sites, the -CIEs in $\delta^{13}C_{org}$ are smaller in amplitude and shorter in duration than those in $\delta^{13}C_{carb}$. However, in the Agost section an unexpected +CIE occurs in the $\delta^{13}C_{org}$ record (but not in the $\delta^{13}C_{carb}$; Fig. 3), and this was also observed by Sepúlveda et al. (2019). Like Sepúlveda et al. (2019) we attribute this to complex post-KPgB inputs of ^{13}C-enriched organic matter, possibly from older reworked organic material being eroded and deposited on the basin. Similar processes could also explain why $\delta^{13}C_{org}$ records at other sites exhibit smaller -CIEs than corresponding $\delta^{13}C_{carb}$.

5.3. Changes in algal and bacterial communities across KPgB

Eukaryote and bacterial biomarkers are present in the Agost section and persist through the event and afterwards. In fact, steranes, hopanes, and *n*-alkanes occur in every sample. There is some evidence for decreased algal production from the decrease in $CaCO_3$ contents, decrease in sterane/hopane ratios and the absence of detectable pristane and phytane in post-KPgB sediments; however, pristane and phytane are also absent from some pre-KPgB sediments and are abundant in samples in unit d. Collectively, these data are consistent with previous biomarker studies wherein disruption of primary production was relatively transient (Bralower et al., 2020; Schaefer et al., 2020; Sepúlveda et al., 2009). This can be further explored via distributions of those compounds.

Changes in the relative contribution of terrigenous OM have implications for the interpretation of sterane biomarker ratios as strictly algal biomarkers, but this does not seem to be the case in the Agost section. For example, we expect elevated higher plant inputs to be associated with elevated proportions of the C_{29} sterane. However, the opposite is observed, i.e. the highest HMW/∑total *n*-alkane ratio is associated with high C_{27} sterane proportions (Fig. 5). Nor do sterane proportions match putative changes in thermal maturity. Therefore, variations in the distribution of steranes and hopanes of different carbon number appear to reflect changes in phytoplankton and bacterial sources, respectively.

Despite the persistence of life across the KPgB, variability in OM inputs does occur across the KPgB at the Agost section. Sterane distributions switch from an assemblage dominated by C_{27} prior to the event to an assemblage dominated by both C_{27} and C_{29} post-KPgB (Fig. 7). There is little variation in C_{28}/C_{29} sterane ratios, however, similar to observations from the Fish Clay in Denmark (Sepúlveda et al., 2009). Although hopane distributions are different before and after the ejecta layer deposition, the dominant hopane is $>C_{31}$ prior the KPgB and $<C_{30}$ afterwards (Table 3c). Therefore, diverse biomarkers persist through the section and their abundances rapidly recover by unit d, but the organic matter assemblage in Danian sediments overlying the ejecta layer is different than that of the late Maastrichtian.

The sterane/hopane ratios [S/(S + H)] vary minimally, by about a factor of 3, with highest ratios in the uppermost parts of unit a and unit d, i.e. the latest Maastrichtian and the Danian post-boundary layer interval. We have compared our [S/(S + H)] ratio with that from the Fish

Clay in Denmark (Sepúlveda et al., 2009), although it is located in a different setting with higher sedimentation rates, with both sections showing a minimum value immediately above the KPgB and maximum values in the uppermost part of the section (Fig. 7). In contrast, value variations of the [S/(S + H)] ratio along the KPgB published by Bralower et al. (2020) from Sites 738 (Kerguelen Plateau) and 1262 (Walvis Ridge), are in agreement with values from Agost, since all are distal and bathyal sections, showing a rapid recovery of bacterial and algal production after the impact (Fig. 7). This likely reflects changes in algal inputs, with a transient decrease post-KPgB followed by a rapid recovery. However, recent work in the Chicxulub core (Schaefer et al., 2020) reveals large changes in bacterial assemblages in the immediate KPgB aftermath, such that the observed changes could be related to the distance to the impact site or could reflect more dynamic variation in both algal and bacterial populations.

In summary, and consistent with previous investigations of non-fossilized communities (i.e. Bralower et al., 2020; Sepúlveda et al., 2009), the Agost section exhibits only modest evidence for a decrease in aquatic productivity in the aftermath of the KPgB. This is reflected by a decline in sterane to hopane ratios and isoprenoid to *n*-alkane ratios, and it is consistent with the decrease in $\%CaCO_3$. Our work, therefore, expands the findings of Sepúlveda et al. (2009) from neritic to bathyal settings. In apparent contrast to the neritic Fish Clay, Agost does record a change in sterane distributions that could document a long-term change in algal assemblages. It is difficult to define exactly what these changes were, but it is possible that either eukaryotic assemblages changed and/or became simpler, hence less variable and more stable. Nonetheless, our results reaffirm the conclusion that the recovery of algal and microbial assemblages occurred relatively rapidly after the KPg extinction event.

6. Conclusions

We have determined the distribution of selected biomarkers (*n*-alkanes, acyclic isoprenoids, steranes and hopanes), C-isotope profiles, TOC content and major and trace elements across the KPgB in the Agost section (SE Spain), throughout a continuous ~32 cm-thick section extending from 5 kyr before to 24 kyr after the event. U_{EF} vs Mo_{EF} covariation, the presence of gammacerane and elevated homohopane indices suggest more reducing conditions just within the KPgB. Biomarker ratios, including those indicative of higher plants (i.e. HMW/$\sum$total *n*-alkane ratios and CPIs) and thermal maturity (but here interpreted as petrogenic input, i.e. ββ/(αα + ββ) sterane and 22S/(22S + 22R) and βα/(βα + αβ) hopane ratios), indicate that the interval immediately preceding the KPgB through to the boundary clay layer was characterized by highly variable terrigenous inputs. This appears to have impacted the bulk organic carbon isotopic record, as observed elsewhere. Most significantly, we observe a transient decrease in eukaryotic (algal) inputs in the boundary clay layer, reflected by both lower $\%CaCO_3$ but also by lower sterane/hopane ratios and linear isoprenoid to *n*-alkane ratios. Therefore, we conclude that, at the Agost distal section, algal and bacterial assemblages were affected by the impact event, but these particular biotic changes were minor and transient. Note that many of these biomarker changes were much smaller than those observed for other biotic events in Earth's history. Furthermore, steranes occurred in all samples, and many biomarker ratios returned to pre-KPgB values by the early Danian, i.e. within 10 kyr. Some biomarker ratios, such as the proportions of C_{27} relative to C_{29} steranes, remained different post-KPgB providing some evidence for a longer-term impact on biotic communities. However, the Agost section biomarker records generally document the persistence of non-fossilized algae and bacteria and a rapid recovery from the KPgB impact. This relatively muted biotic response is likely because Agost is distant from the impact crater.

Author declaration

We wish to confirm that there are no known conflicts of interest associated with this publication and there has been no significant financial support for this work that could have influenced its outcome.

We confirm that the manuscript has been read and approved by all named authors and that there are no other persons who satisfied the criteria for authorship but are not listed. We further confirm that the order of authors listed in the manuscript has been approved by all of us.

We confirm that we have given due consideration to the protection of intellectual property associated with this work and that there are no impediments to publication, including the timing of publication, with respect to intellectual property. In so doing we confirm that we have followed the regulations of our institutions concerning intellectual property.

We understand that the Corresponding Author is the sole contact for the Editorial process (including Editorial Manager and direct communications with the office). She is responsible for communicating with the other authors about progress, submissions of revisions and final approval of proofs. We confirm that we have provided a current, correct email address which is accessible by the Corresponding Author and which has been configured to accept email from (claudia.sosamontesdeoca@bristol.ac.uk).

Declaration of Competing Interest

The authors declare that they have no known competing financial interests or personal relationships that could have appeared to influence the work reported in this paper.

Acknowledgments

This research was funded through Projects CGL2012-33281, CGL2012-32659, CGL2014-55274P, CGL2015-66835-P, PID2019-104625RB-100 (Secretaría de Estado de I+D+i, Spain), Projects RNM-05212, P18-RT-3804, P18-RT-4074 and Research Groups RNM-178, RNM-179 and RNM-200 (Junta de Andalucía), Project B-RNM-072-UGR18 (FEDER Andalucía) and the Scientific Excellence Unit UCE-2016-05 (Universidad de Granada). R.D.P. acknowledges funding from the advanced ERC Grant "The Greenhouse Earth System" (T-GRES, project reference 340923). C.S.M.O. acknowledges post-doctoral fellowship from the University of Granada and a Newton International post-doctoral fellowship from Royal Society (project reference NIF\R1\191430). M.R.G. acknowledges post-doctoral fellowships from the University of Jaén and Juan de la Cierva-Incorporación program in the University of Granada from Secretaría de Estado de I + D + i, Spain (IJCI-2017-33755). We are grateful to Editor Shucheng Xie, and both anonymous reviewers, for their valuable comments and suggestions.

References

Algeo, T.J., Tribovillard, N., 2009. Environmental analysis of paleoceanographic systems based on molybdenum-uranium covariation. Chem. Geol. 268, 211–225. https://doi.org/10.1016/j.chemgeo.2009.09.001.

Alvarez, L.W., Alvarez, W., Asaro, F., Michel, H.V., 1980. Extraterrestrial cause for the Cretaceous-Tertiary extinction. Science 208, 1095–1108.

Alvarez, W., Asaro, F., Montanari, A., 1990. Iridium profile for 10 million years across the Cretaceous-Tertiary boundary at Gubbio (Italy). Science 250, 1700–1702.

Alvarez, S.A., Gibbs, S.J., Bown, P.R., Kim, H., Sheward, R.M., Ridgwell, A., 2019. Diversity decoupled from ecosystem function and resilience during mass extinction recovery. Nature 574, 242–245. https://doi.org/10.1038/s41586-019-1590-8.

Artemieva, N., Morgan, J., 2009. Modeling the formation of the K-Pg boundary layer. Icarus 201, 768–780. https://doi.org/10.1016/j.icarus.2009.01.021.

Belin, B.J., Busset, N., Giraud, E., Molinaro, A., Silipo, A., Newman, D.K., 2018. Hopanoid lipids: from membranes to plant-bacteria interactions. Nat. Rev. Microbiol. 16, 304–315. https://doi.org/10.1038/nrmicro.2017.173.

Birch, H.S., Coxall, H.K., Pearson, P.N., Kroon, D., Schmidt, D.N., 2016. Partial collapse of the marine carbon pump after the Cretaceous-Paleogene boundary. Geology 44, 287–290. https://doi.org/10.1130/G37581.1.

Bishop, A.N., Farrimond, P., 1995. A new method of comparing extended hopane distributions. Org. Geochem. 23, 987–990. https://doi.org/10.1016/0146-6380(95)00074-7.

Bralower, T.J., Cosmidis, J., Heaney, P.J., Kump, L.R., Morgan, J.V., Harper, D.T., Lyons, S.L., Freeman, K.H., Grice, K., Wendler, J.E., Zachos, J.C., Artemieva, N., Chen, S.A., Gulick, S.P.S., House, C.H., Jones, H.L., Lowery, C.M., Nims, C., Schaefer, B., Thomas, E., Vajda, V., 2020. Origin of a global carbonate layer deposited in the aftermath of the Cretaceous-Paleogene boundary impact. Earth Planet. Sci. Lett. 548, 116476 https://doi.org/10.1016/j.epsl.2020.116476.

Bray, E.E., Evans, E.D., 1961. Distribution of n-paraffins as a clue to recognition of source beds. Geochim. Cosmochim. Acta 22, 2–15. https://doi.org/10.1016/0016-7037(61)90069-2.

Calvert, S.E., Pedersen, T.F., 1993. Geochemistry of recent oxic and anoxic marine sediments: Implications for the geological record. Mar. Geol. 113, 67–88.

Carmichael, M.J., Pancost, R.D., Lunt, D.J., 2018. Changes in the occurrence of extreme precipitation events at the Paleocene–Eocene thermal maximum. Earth Planet. Sci. Lett. 501, 24–36. https://doi.org/10.1016/j.epsl.2018.08.005.

Castro, J.M., de Gea, G.A., Quijano, M.L., Aguado, R., Froehner, S., Naafs, B.D.A., Pancost, R.D., 2019. Complex and protracted environmental and ecological perturbations during OAE 1a - evidence from an expanded pelagic section from south Spain (Western Tethys). Glob. Planet. Chang. 183, 103030. https://doi.org/10.1016/j.gloplacha.2019.103030.

Clyde, W.C., Ramezani, J., Johnson, K.R., Bowring, S.A., Jones, M.M., 2016. Direct high-precision U–Pb geochronology of the end-Cretaceous extinction and calibration of Paleocene astronomical timescales. Earth Planet. Sci. Lett. 452, 272–280. https://doi.org/10.1016/j.epsl.2016.07.041.

Cranwell, P.A., Eglinton, G., Robinson, N., 1987. Lipids of aquatic organisms as potential contributors to lacustrine sediments-II. Org. Geochem. 11, 513–527. https://doi.org/10.1016/0146-6380(87)90007-6.

De Lange, G.J., Van der Sloot, H.A., Wijkstra, J., 1987. Implications of the diagenetic mobility of Ir for the interpretation of the anomaly at the K/T boundary. Geol. Soc. Spec. Publ. 31, 147–165.

D'Hondt, S., 2005. Consequences of the Cretaceous/Paleogene Mass extinction for marine ecosystems. Annu. Rev. Ecol. Evol. Syst. 36, 295–317. https://doi.org/10.1146/annurev.ecolsys.35.021103.105715.

Didyk, B.M., Simoneit, B.R.T., Brassell, S.C., Eglinton, G., 1978. Organic geochemical indicators of palaeoenvironmental conditions of sedimentation. Nature 272, 216–222. https://doi.org/10.1038/272216a0.

Eglinton, T.I., Eglinton, G., 2008. Molecular proxies for paleoclimatology. Earth Planet. Sci. Lett. 275, 1–16. https://doi.org/10.1016/j.epsl.2008.07.012.

Eglinton, G., Hamilton, R.J., 1963. The distribution of *n*-alkanes. In: Swain, T. (Ed.), Chemical Plant Taxonomy. Academic Press, London, pp. 87–217.

Eglinton, G., Hamilton, R.J., 1967. Leaf epicuticular waxes. Science 156. https://doi.org/10.1126/science.156.3780.1322, 1322 LP – 1335.

Gearing, P., Gearing, J.N., Lytle, T.F., Lytle, J.S., 1976. Hydrocarbons in 60 northeast Gulf of Mexico shelf sediments: a preliminary survey. Geochim. Cosmochim. Acta 40, 1005–1017. https://doi.org/10.1016/0016-7037(76)90043-0.

Gelin, F., Kok, M.D., De Leeuw, J.W., Sinninghe Damsté, J.S., 1998. Laboratory sulfurisation of the marine microalga Nannochloropsis salina. Org. Geochem. 29, 1837–1848. https://doi.org/10.1016/S0146-6380(98)00171-5.

Gelin, F., Volkman, J.K., Largeau, C., Derenne, S., Sinninghe Damsté, J.S., De Leeuw, J.W., 1999. Distribution of aliphatic, nonhydrolyzable biopolymers in marine microalgae. Org. Geochem. 30, 147–159. https://doi.org/10.1016/S0146-6380(98)00206-X.

Gelpi, E., Schneider, H., Mann, J., Oro, J., 1970. Hydrocarbons of geochemical significance in microscopic algae. Phytochemistry 9 (3), 603–612.

Glass, B.p., Burns, C.A., 1987. Late eocene crystal-bearing spherules - 2 layers or one - a reply. Meteoritics 23, 265–279.

Goderis, S., Tagle, R., Belza, J., Smit, J., Montanari, A., Vanhaecke, F., Erzinger, J., Claeys, P., 2013. Reevaluation of siderophile element abundances and ratios across the Cretaceous-Paleogene (K-Pg) boundary: Implications for the nature of the projectile. Geochim. Cosmochim. Acta 120, 417–446. https://doi.org/10.1016/j.gca.2013.06.010.

Grice, K., Cao, C., Love, G.D., Böttcher, M.E., Twitchett, R.J., Grosjean, E., Summons, R. E., Turgeon, S.C., Dunning, W., Jin, Y., 2005. Photic zone euxinia during the permian-triassic superanoxic event. Science 307, 706–709. https://doi.org/10.1126/science.1104323.

Groot, J.J., de Jonge, R.B.G., Langereis, C.G., ten Kate, W.G.H.Z., Smit, J., 1989. Magnetostratigraphy of the Cretaceous-Tertiary boundary at Agost (Spain). Earth Planet. Sci. Lett. 94, 385–397. https://doi.org/10.1016/0012-821X(89)90155-6.

Gulick, S.P.S., Bralower, T.J., Ormö, J., Hall, B., Grice, K., Schaefer, B., Lyons, S., Freeman, K.H., Morgan, J.V., Artemieva, N., Kaskes, P., De Graaff, S.J., Whalen, M. T., Collins, G.S., Tikoo, S.M., Verhagen, C., Christeson, G.L., Claeys, P., Coolen, M.J. L., Goderis, S., Goto, K., Grieve, R.A.F., McCall, N., Osinski, G.R., Rae, A.S.P., Riller, U., Smit, J., Vajda, V., Wittmann, A., 2019. The first day of the Cenozoic. Proc. Natl. Acad. Sci. U. S. A. 116, 19342–19351. https://doi.org/10.1073/pnas.1909479116.

Hackley, P.C., Zhang, T., Jubb, A.M., Valentine, B.J., Dulong, F.T., Hatcherian, J.J., 2020. Organic petrography of Leonardian (Wolfcamp A) mudrocks and carbonates, Midland Basin, Texas: the fate of oil-prone sedimentary organic matter in the oil window. Mar. Pet. Geol. 112, 104086 https://doi.org/10.1016/j.marpetgeo.2019.104086.

Hildebrand, A.R., Penfield, G.T., Kring, D.A., Pilkington, M., A., C.Z., Jacobsen, S.B., Boynton, W.V., 1991. Chicxulub Crater: a possible Cretaceous/Tertiary boundary impact crater on the Yucatán Peninsula, Mexico. Geology 19, 867. https://doi.org/10.1130/0091-7613(1991)019<0867:CCAPCT>2.3.CO;2.

Hull, P., Bornemann, A., Penman, D., Henehan, M., Norris, R., Wilson, P., Blum, P., Alegret, L., Batenburg, S., Bown, P., Bralower, T., Cournede, C., Deutsch, A., Donner, B., Friedrich, O., Jehle, S., Kim, H., Kroon, D., Lippert, P., Loroch, D., Moebius, I., Moriya, K., Peppe, D., Ravizza, G., Röhl, U., Schueth, J., Sepúlveda, J., Sexton, P., Sibert, E., S, K., Summons, R., Thomas, E., Westerhold, T., Whiteside, J., Yamaguchi, T., Zachos, J., 2020. On impact and volcanism across the Cretaceous-Paleogene boundary. Science 367, 266–272.

Kennicutt, M.C., Barker, C., Brooks, J.M., DeFreitas, D.A., Zhu, G.H., 1987. Selected organic matter source indicators in the Orinoco, Nile and Changjiang deltas. Org. Geochem. 11, 41–51. https://doi.org/10.1016/0146-6380(87)90050-7.

Kyte, F.T., 1998. A meteorite from the cretaceous/Tertiary boundary. Nature 396, 237–239.

Laska, W., Rodríguez-Tovar, F.J., Uchman, A., 2017. Evaluating macrobenthic response to the Cretaceous–Palaeogene event: a high-resolution ichnological approach at the Agost section (SE Spain). Cretac. Res. 70, 96–110. https://doi.org/10.1016/j.cretres.2016.10.003.

Lowery, C.M., Bralower, T.J., Owens, J.D., Rodríguez-tovar, F.J., Jones, H., Smit, J., Gulick, S., Joanna, V., Green, S., Chenot, E., Whalen, M.T., Claeys, P., Farley, K., Sean, P., 2018. Rapid recovery of life at ground zero of the end-Cretaceous mass extinction. Nature. https://doi.org/10.1038/s41586-018-0163-6.

Lowery, C.M., Bown, P.R., Fraass, A.J., Hull, P.M., 2020. Ecological response of plankton to environmental change: thresholds for extinction Christopher. Annu. Rev. Earth Planet. Sci. 48 https://doi.org/10.1146/annurev-earth-081619-052818, 16.1–16.27.

Lyons, S.L., Karp, A.T., Bralower, T., Grice, K., Schaefer, B., Gulick, S.P.S., Morgan, J.V., Freeman, K.H., 2020. Organic matter from the Chicxulub crater exacerbated the K-Pg impact winter. Proc. Natl. Acad. Sci. U. S. A. 117, 25327–25334. https://doi.org/10.1073/pnas.2004596117.

Mackenzie, A.S., Patience, R.L., Maxwell, J.R., Vandenbroucke, M., Durand, B., 1980. Molecular parameters of maturation in the Toarcian shales, Paris Basin, France—I. changes in the configurations of acyclic isoprenoid alkanes, steranes and triterpanes. Geochim. Cosmochim. Acta 44, 1709–1721. https://doi.org/10.1016/0016-7037(80)90222-7.

Martínez-Ruiz, F., Ortega-Huertas, M., Palomo, I., Acquafredda, P., 1997. Quench textures in altered spherules from the Cretaceous-Tertiary boundary layer at Agost and Caravaca, SE Spain. Sediment. Geol. 113, 137–147. https://doi.org/10.1016/S0037-0738(97)00057-2.

Mazurek, M., Simoneit, B.R., 1984. Characterization of biogenic and petroleum-derived organic matter in aerosols over remote, rural and urban areas. In: Identif and Anal of Org Pollut in Air, pp. 353–370.

Mizukami, T., Kaiho, K., Oba, M., 2013. Significant changes in land vegetation and oceanic redox across the Cretaceous/Paleogene boundary. Palaeogeogr. Palaeoclimatol. Palaeoecol. 369, 41–47. https://doi.org/10.1016/j.palaeo.2012.09.020.

Mizukami, T., Kaiho, K., Oba, M., 2014. A spike of woody plant biomarkers in the deep-sea iridium layer at the Cretaceous/Paleogene boundary. Palaeogeogr. Palaeoclimatol. Palaeoecol. 412, 241–248. https://doi.org/10.1016/j.palaeo.2014.07.041.

Molina, E., Alegret, L., Arenillas, I., Arz, J.A., 2005. The Cretaceous/Paleogene boundary at the Agost section revisited : paleoenvironmental reconstruction and mass extinction pattern. J. Iber. Geol. 31, 135–148.

Morford, J.L., Emerson, S., 1999. The geochemistry of redox sensitive trace metals in sediments. Geochim. Cosmochim. Acta 63, 1735–1750. https://doi.org/10.1016/S0016-7037(99)00126-X.

Pälike, H., 2013. Impact and Extinction. Science 339, 655–656.

Pendoley, K., 1992. Hydrocarbons in Rowley Shelf (Western Australia) oysters and sediments. Mar. Pollut. Bull. 24, 210–215. https://doi.org/10.1016/0025-326X(92)90532-B.

Peters, K.E., Moldowan, J.M., 1991. Effects of source, thermal maturity, and biodegradation on the distribution and isomerization of homohopanes in petroleum. Org. Geochem. 17, 47–61. https://doi.org/10.1016/0146-6380(91)90039-M.

Peters, K.E., Peters, K.E., Walters, C.C., Moldowan, J.M., 2005. The Biomarker Guide. Cambridge University Press.

Poynter, J., Eglinton, G., 1990. Molecular composition of three sediments from hole 717C: the Bengal Fan. Proc., Sci. results. In: ODP, Leg 116, distal Bengal Fan, 116, pp. 155–161. https://doi.org/10.2973/odp.proc.sr.116.151.1990.

Quijano, M.L., Castro, J.M., Pancost, R.D., de Gea, G.A., Najarro, M., Aguado, R., Rosales, I., Martín-Chivelet, J., 2012. Organic geochemistry, stable isotopes, and facies analysis of the Early Aptian OAE-New records from Spain (Western Tethys). Palaeogeogr. Palaeoclimatol. Palaeoecol. 365–366, 276–293. https://doi.org/10.1016/j.palaeo.2012.09.033.

Renne, P.R., Deino, A.L., Hilgen, F.J., Kuiper, K.F., Mark, D.F., Mitchell, W.S., Morgan, L. E., Mundil, R., Smit, J., 2013. Time scales of critical events around the Cretaceous-Paleogene boundary. Science 339, 684–687. https://doi.org/10.1126/science.1230492.

Rodríguez-Tovar, F.J., 2005. Fe-oxide spherules infilling Thalassinoides burrows at the Cretaceous-Paleogene (K-P) boundary: evidence of a near-contemporaneous macrobenthic colonization during the K-P event. Geology 33, 585–588. https://doi.org/10.1130/G21527.1.

Rodríguez-Tovar, F.J., Uchman, A., 2004. Ichnotaxonomic analysis of the Cretaceous/Palaeogene boundary interval in the Agost section, south-east Spain. Cretac. Res. 25, 635–647. https://doi.org/10.1016/j.cretres.2004.06.003.

Rodríguez-Tovar, F.J., Uchman, A., 2006. Ichnological analysis of the Cretaceous-Palaeogene boundary interval at the Caravaca section, SE Spain. Palaeogeogr. Palaeoclimatol. Palaeoecol. 242, 313–325. https://doi.org/10.1016/j.palaeo.2006.06.006.

Rodríguez-Tovar, F.J., Martínez-Ruiz, F., Bernasconi, S.M., 2004. Carbon isotope evidence for the timing of the Cretaceous-Palaeogene macrobenthic colonisation at the Agost section (southeast Spain). Palaeogeogr. Palaeoclimatol. Palaeoecol. 203, 65–72. https://doi.org/10.1016/S0031-0182(03)00660-6.

Rodríguez-Tovar, F.J., Martínez-Ruiz, F., Bernasconi, S.M., 2006. Use of high-resolution ichnological and stable isotope data for assessing completeness of a K-P boundary section, Agost, Spain. Palaeogeogr. Palaeoclimatol. Palaeoecol. 237, 137–146. https://doi.org/10.1016/j.palaeo.2005.11.019.

Rodríguez-Tovar, F., Lowery, C., Bralower, T., Gulick, S., Jones, H., 2020. Rapid macrobenthic diversification and stabilization after the end-Cretaceous mass extinction event. Geology XX, 1–5. https://doi.org/10.1130/G47589.1.

Rohmer, M., Bouvier-Nave, P., Ourisson, G., 1984. Distribution of hopanoid triterpenes in prokaryotes. J. Gen. Microbiol. 130, 1137–1150. https://doi.org/10.1099/00221287-130-5-1137.

Scasso, R.A., Concheyro, A., Aberhan, M., Hecht, L., Medina, F.A., Tagle, R., 2005. A tsunami deposit at the Cretaceous/Paleogene boundary in the Neuquén Basin of Argentina. Cretac. Res. 26, 283–297. https://doi.org/10.1016/j.cretres.2004.12.003.

Scasso, R.A., Prámparo, M.B., Vellekoop, J., Franzosi, C., Castro, L.N., Sinninghe Damsté, J.S., 2020. A high-resolution record of environmental changes from a Cretaceous-Paleogene section of Seymour Island, Antarctica. Palaeogeogr. Palaeoclimatol. Palaeoecol. 555, 109844 https://doi.org/10.1016/j.palaeo.2020.109844.

Schaefer, B., Grice, K., Coolen, M.J.L., Summons, R.E., Cui, X.X., Bauersachs, T., Schwark, L., Böttcher, M.E., Bralower, T.J., Lyons, S.L., Freeman, K.H., Cockell, C.S., Gulick, S.S., Morgan, J.V., Whalen, M.T., Lowery, C.M., Vajda, V., 2020. Microbial life in the nascent chicxulub crater. Geology 48, 1–5. https://doi.org/10.3997/2214-4609.201902850.

Schefuß, E., Ratmeyer, V., Stuut, J.B.W., Jansen, J.H.F., Sinninghe Damsté, J.S., 2003. Carbon isotope analyses of n-alkanes in dust from the lower atmosphere over the central eastern Atlantic. Geochim. Cosmochim. Acta 67, 1757–1767. https://doi.org/10.1016/S0016-7037(02)01414-X.

Schoene, B., Samperton, K.M., Eddy, M.P., Keller, G., Adatte, T., Bowring, S.A., Khadri, S. F.R., Gertsch, B., 2015. U-Pb geochronology of the Deccan Traps and relation to the end-Cretaceous mass extinction. Science 347, 182–184. https://doi.org/10.1126/science.aaa0118.

Schoene, B., Eddy, M.P., Samperton, K.M., Keller, C.B., Keller, G., Adatte, T., Khadri, S.F. R., 2019. U-Pb constraints on pulsed eruption of the Deccan Traps across the end-Cretaceous mass extinction. Science 363, 862–866. https://doi.org/10.1126/science.aau2422.

Schulte, P., Alegret, L., Arenillas, I., Arz, J.A., Barton, P.J., Bown, P.R., Bralower, T.J., Christeson, G.L., Claeys, P., Cockell, C.S., Collins, G.S., Deutsch, A., Goldin, T.J., Goto, K., Grajales-Nishimura, J.M., Grieve, R.A.F., Gulick, S.P.S., Johnson, K.R., Kiessling, W., Koeberl, C., Kring, D.A., MacLeod, K.G., Matsui, T., Melosh, J., Montanari, A., Morgan, J.V., Neal, C.R., Nichols, D.J., Norris, R.D., Pierazzo, E., Ravizza, G., Rebolledo-Vieyra, M., Reimold, W.U., Robin, E., Salge, T., Speijer, R.P., Sweet, A.R., Urrutia-Fucugauchi, J., Vajda, V., Whalen, M.T., Willumsen, P.S., 2010. The chicxulub asteroid impact and mass extinction at the cretaceous-paleogene boundary. Science 327, 1214–1218. https://doi.org/10.1126/science.1177265.

Schwark, L., Empt, P., 2006. Sterane biomarkers as indicators of palaeozoic algal evolution and extinction events. Palaeogeogr. Palaeoclimatol. Palaeoecol. 240, 225–236. https://doi.org/10.1016/j.palaeo.2006.03.050.

Seifert, W.K., Moldowan, J.M., 1980. The effect of thermal stress on source-rock quality as measured by hopane stereochemistry. Phys. Chem. Earth 12, 229–237. https://doi.org/10.1016/0079-1946(79)90107-1.

Sepúlveda, J., Wendler, J.E., Summons, R.E., Hinrichs, K.-U., 2009. Rapid Resurgence of Marine Productivity after the Cretaceous-Paleogene Mass Extinction. Science 326, 129–132. https://doi.org/10.1126/science.1176233.

Sepúlveda, J., Alegret, L., Thomas, E., Haddad, E., Cao, C., Summons, R.E., 2019. Stable isotope constraints on marine productivity across the cretaceous-paleogene mass extinction. Paleoceanogr. Paleoclimatol. 34, 1195–1217. https://doi.org/10.1029/2018PA003442.

Shukolyukov, A., Lugmair, G.W., 2004. Manganese-chromium isotope systematics of enstatite meteorites. Geochim. Cosmochim. Acta 68, 2875–2888. https://doi.org/10.1016/j.gca.2004.01.008.

Sinninghe-Damste, J.S., Kenig, F., Koopmans, M.P., Schouten, S., Hayes, J.M., De Leeljw, J.W., 1995. Evidence for gammacerane. Geochim. Cosmochim. Acta 59, 1895–1900.

Smit, J., 1999. The global stratigraphy of the Cretaceous-Tertiary boundary impact ejecta. Annu. Rev. Earth Planet. Sci. 27, 75–113.

Smit, J., Klaver, G., 1981. Sanidine spherules at the Cretaceous-Tertiary boundary indicate a large impact event. Nature 292, 47–49.

Sosa-Montes de Oca, C., 2018. Environmental Changes Across the Cretaceous/Palaeogene Boundary: A High Resolution Approach for Reconstructiong Eco-Sedimentary Conditions. Universidad de Granada.

Sosa-Montes de Oca, C., Martínez-Ruiz, F., Rodríguez-Tovar, F.J., 2013. Bottom-water conditions in a marine basin after the Cretaceous-Paleogene impact event: timing the recovery of oxygen levels and productivity. PLoS One 8, e82242. https://doi.org/10.1371/journal.pone.0082242.

Sosa-Montes de Oca, C., Rodríguez-Tovar, F.J., Martínez-Ruiz, F., 2016. Geochemical and isotopic characterization of trace fossil infillings: New insights on tracemaker activity after the K/Pg impact event. Cretac. Res. 57, 391–401. https://doi.org/10.1016/j.cretres.2015.03.003.

Sosa-Montes de Oca, C., Rodríguez-Tovar, F.J., Martínez-Ruiz, F., Monaco, P., 2017. Paleoenvironmental conditions across the Cretaceous–Paleogene transition at the Apennines sections (Italy): an integrated geochemical and ichnological approach. Cretac. Res. 71 https://doi.org/10.1016/j.cretres.2016.11.005.

Sosa-Montes de Oca, C., de Lange, G.J., Martínez-Ruiz, F., Rodríguez-Tovar, F.J., 2018a. Application of laser ablation-ICP-MS to determine high-resolution elemental profiles across the Cretaceous/Paleogene boundary at Agost (Spain). Palaeogeogr. Palaeoclimatol. Palaeoecol. 497, 128–138. https://doi.org/10.1016/j.palaeo.2018.02.012.

Sosa-Montes de Oca, C., Claudia, de Lange, J., G., Martínez-Ruiz, F., Rodríguez-Tovar, F. J., 2018b. High-resolution data from Laser Ablation-ICP-MS and by ICP-OES analyses at the Cretaceous/Paleogene boundary section at Agost (SE Spain). Data Br. 18, 1900–1906. https://doi.org/10.1016/j.dib.2018.04.118.

Sosa-Montes de Oca, C., de Lange, G.J., Martínez-Ruiz, F., Ortega-Huertas, M., Rodríguez-Tovar, F.J., 2020. Microscale trace-element distribution across the Cretaceous/Palaeogene ejecta layer at the Agost section: Constraining the recovery of pre-impact conditions. Chem. Geol. 533 https://doi.org/10.1016/j.chemgeo.2019.119431.

Sprain, C.J., Renne, P.R., Vanderkluysen, L., Pande, K., Self, S., Mittal, T., 2019. The eruptive tempo of deccan volcanism in relation to the cretaceous-paleogene boundary. Science 363, 866–870. https://doi.org/10.1126/science.aav1446.

Taylor, K.W.R., Willumsen, P.S., Hollis, C.J., Pancost, R.D., 2018. South Pacific evidence for the long-term climate impact of the Cretaceous/Paleogene boundary event. Earth Sci. Rev. 179, 287–302. https://doi.org/10.1016/j.earscirev.2018.02.012.

Tegelaar, E.W., de Leeuw, J.W., Derenne, S., Largeau, C., 1989. A reappraisal of kerogen formation. Geochim. Cosmochim. Acta 53, 3103–3106. https://doi.org/10.1016/0016-7037(89)90191-9.

Ten Haven, H.L., De Leeuw, J.W., Rullkötter, J., Damsté, J.S.S., 1987. Restricted utility of the pristane/phytane ratio as a palaeoenvironmental indicator. Nature 330, 641–643. https://doi.org/10.1038/330641a0.

Tribovillard, N., Algeo, T.J., Lyons, T., Riboulleau, A., 2006. Trace metals as paleoredox and paleoproductivity proxies: an update. Chem. Geol. 232, 12–32. https://doi.org/10.1016/j.chemgeo.2006.02.012.

Tribovillard, N., Algeo, T.J., Baudin, F., Riboulleau, A., 2012. Analysis of marine environmental conditions based onmolybdenum-uranium covariation-applications to Mesozoic paleoceanography. Chem. Geol. 324–325, 46–58. https://doi.org/10.1016/j.chemgeo.2011.09.009.

van Breugel, Y., Schouten, S., Tsikos, H., Erba, E., Price, G.D., Damsté, J.S.S., 2007. Synchronous negative carbon isotope shifts in marine and terrestrial biomarkers at the onset of the early Aptian oceanic anoxic event 1a: evidence for the release of 13C-depleted carbon into the atmosphere. Paleoceanography 22, 1–13. https://doi.org/10.1029/2006PA001341.

Van der Weijden, C.H., 2002. Pitfalls of normalization of marine geochemical data using a common divisor. Mar. Geol. 184, 167–187.

Van Hinsbergen, D.J.J., De Groot, L., Van Schaik, S.J., Spakman, W., Bijl, P.K., Sluijs, A., Langereis, C.G., Brinkhuis, H., 2015. A paleolatitude calculator for paleoclimate studies. PLoS One 10, 1–21. https://doi.org/10.1371/journal.pone.0126946.

Vellekoop, J., Sluijs, A., Smit, J., Schouten, S., Weijers, J.W.H., Sinninghe Damste, J.S., Brinkhuis, H., 2014. Rapid short-term cooling following the Chicxulub impact at the Cretaceous-Paleogene boundary. Proc. Natl. Acad. Sci. U. S. A. 1–5. https://doi.org/10.1073/pnas.1319253111.

Vellekoop, J., Smit, J., van de Schootbrugge, B., Weijers, J.W.H., Galeotti, S., Sinninghe Damste, J.S., Brinkhuis, H., 2015. Palynological evidence for prolonged cooling along the Tunisian continental shelf following the K-Pg boundary impact. Palaeogeogr. Palaeoclimatol. Palaeoecol. 426, 216–228. https://doi.org/10.1016/j.palaeo.2015.03.021.

Vellekoop, J., Esmeray-Senlet, S., Miller, K.G., Browning, J.V., Sluijs, A., van de Schootbrugge, B., Sinninghe Damste, J.S., Brinkhuis, H., 2016. Evidence for Cretaceous-Paleogene boundary bolide "impact winter" conditions from New Jersey, USA. Geology 44, 619–622. https://doi.org/10.1130/G37961.1.

Vellekoop, J., Woelders, L., Sluijs, A., Miller, K.G., Speijer, R.P., 2019. Phytoplankton community disruption caused by latest Cretaceous global warming. Biogeosciences 16, 4201–4210. https://doi.org/10.5194/bg-16-4201-2019.

Volkman, J.K., Barrett, S.M., Blackburn, S.I., Mansour, M.P., Sikes, E.L., Gelin, F., 1998. Microalgal biomarkers: a review of recent research developments. Org. Geochem. 29, 1163–1179. https://doi.org/10.1016/S0146-6380(98)00062-X.

Xie, S., Pancost, R.D., Huang, J., Wignall, P.B., Yu, J., Tang, X., Chen, L., Huang, X., Lai, X., 2007. Changes in the global carbon cycle occurred as two episodes during the Permian-Triassic crisis. Geology 35, 1083–1086. https://doi.org/10.1130/G24224A.1.

Xie, S., Pancost, R.D., Wang, Y., Yang, H., Wignall, P.B., Luo, G., Jia, C., Chen, L., 2010. Cyanobacterial blooms tied to volcanism during the 5 m.y. Permo-Triassic biotic crisis. Geology 38, 447–450. https://doi.org/10.1130/G30769.1.

Zhou, L., Wignall, P.B., Su, J., Feng, Q., Xie, S., Zhao, L., Huang, J., 2012. U/Mo ratios and δ95/95Mo as local and global redox proxies during mass extinction events. Chem. Geol. 324–325, 99–107. https://doi.org/10.1016/j.chemgeo.2012.03.020.